THE STUDY OF WALL INTERACTIONS OF SPIN POLARIZED RUBIDIUM

ATOMS USING THE FREQUENCY SHIFT IN THE ELECTRON

PARAMAGNETIC RESONANCE OF THE RUBIDIUM ATOMS

BY EMILY JOY ULANSKI

A Dissertation submitted to the

Graduate School-Newark

Rutgers, The State University of New Jersey

in partial fulfillment of the requirements

for the degree of

Doctor of Philosophy

Graduate Program in Applied Physics

written under the direction of

Zhen Wu

and approved by

_____

_____

_____

_____

_____

Newark, New Jersey

May, 2014

©[2014]

Emily Joy Ulanski

ALL RIGHTS RESERVED

ABSTRACT OF THE DISSERTATION

The Study of Wall Interactions of Spin Polarized Rubidium Atoms Using the

Frequency Shift in the Electron Paramagnetic Resonance of the Rubidium Atoms

by Emily Ulanski

Dissertation Director:

Zhen Wu

I studied the effect of wall collisions on the electron paramagnetic resonance (EPR) of

gas phase alkali metal atoms (^{87}Rb). Two types of walls were studied: antirelaxation-

coated walls and RbH-coated walls. I measured the dwell times of spin polarized

Rb atoms on the two most common antirelaxation coatings, octadecyltrichlorosilane

(OTS)- and paraffin. I found that at a cell temperature of 72°C the dwell times for

OTS- and paraffin-coated walls are 0.9 ± 0.1 μs and 1.8 ± 0.2 μs, respectively. The

implication of these dwell times, which are much longer than what was previously

reported in the literature, is discussed in connection with the relaxing property of

these coatings. In cells coated with RbH salt I made the first observation of the

EPR frequency shift of the gas phase ^{87}Rb atoms. Due to collisions with the RbH

salt, which was nuclear spin polarized by spin exchange with optically pumped Rb

vapor. The measured EPR frequency shifts are of the order of several hundred Hz

in a millimeter-sized cell. By measuring the dependence of the EPR frequency shifts

on cell length and by comparing the EPR frequency shifts in RbH-coated cells with those in OTS-coated cells, I provided convincing evidence that the observed EPR frequency shifts are due to collisions with RbH-coated walls, and not due to gas phase processes. The EPR frequency shift is due to the Fermi contact interaction between the s-electron of the adsorbed ^{87}Rb atom and the polarized nucleus on the salt surface. The measured EPR frequency shifts allowed me to calculate the ensemble-averaged phase shift $\delta\phi_s$ experienced by the Rb atom while adsorbed on the walls. Under our experimental condition $\delta\phi_s$ is about 70 mrad. My experiment opens up the possibility of studying surface NMR using gas phase EPR. The phase shift $\delta\phi_s$ is proportional to the surface nuclear polarization, thus provides an interesting method for measuring the surface nuclear polarization using gas phase EPR. My observation will alert the high precision miniature atomic magnetometry community that collisions with cell walls may cause a systematic error and line broadening in the magnetic resonance frequency.

iv

Dedicated to Nanny

Contents

Chapter 1

Introduction

1.1 Magnetic Resonance and Frequency Shifts

Long spin relaxation time of alkali atoms is important in many areas of atomic physics. In optical pumping experiments the surface interaction of optically pumped alkali atoms is one of the main causes of depolarization of optically pumped atoms.

Magnetic resonances are widely used in atomic physics, for example, they are used in precision measurements of magnetic moments. Calaprice et. al. used the spin exchange method to polarize radioactive nuclei ^{133}Xe, ^{133}Xe^m and ^{131}Xe^m [1]. Since these nuclei have very long relaxation times of the order of several minutes, the magnetic resonance linewidths are exceedingly small, allowing for the measurement of their magnetic moments with high precision.

Nuclear magnetic resonance of protons has been used in medicine for magnetic

resonance imaging (MRI) for decades. Recently, nuclear spin polarized inert gas atoms such as xenon and helium have found interesting applications in lung imaging in medicine [3, 4].

Magnetic resonance is also the basis of magnetometry [8]. The sensitivity of the magnetometer depends on the magnetic resonance linewidths. The most important line broadening mechanism due to the gas phase process is the spin exchange broadening. The broadening due to spin exchange can be eliminated using a method proposed by Happer and Tang in 1972 and recently demonstrated by Romalis et. al. [9]. The method is based on the fact that the Larmor frequencies of the $F = 2$ and $F = 1$ levels in an alkali atom have the same magnitude but opposite sign (see section 2.3.1). When the alkali metal density is sufficiently high and the spin exchange collision rate is sufficiently fast, the rate of transfer of the alkali atoms back and forth between the $F = 1$ and $F = 2$ levels will be sufficiently rapid so that they will effectively precess with a single Larmor frequency, thus completely eliminating the broadening due to spin exchange collisions.

In contrast to the relaxation due to gas phase processes, the relaxation due to wall collisions increases with decreasing cell size, and therefore is important for miniature atomic devices, for which there has been much interest such as the recent development of miniature atomic magnetometers [11–13]. Wall relaxation can be greatly reduced by coating the surface of the cell with antirelaxation coatings. Antirelaxation coatings have been used to reduce wall relaxation in atomic clocks [14], magnetometers [10,

15, 16], and fundamental symmetry studies [17]. These coatings have been shown to allow the atoms to collide many more times with the surface, up to 10,000 times for paraffin-coated walls [18] and up to 1,000 times for OTS-coated walls [19, 20], than when the surfaces are not coated. Intensive studies of antirelaxation coatings have been carried out by many groups, hoping to have a better understanding as to why some antirelaxation coatings are better than others. Despite all these studies of antirelaxation coatings, antirelaxation coatings remain an art to a certain degree. For example, when similar coating procedures are used, the reproducibility is poor.

Besides line broadening, magnetic resonance frequency can also be shifted. It is important to understand the mechanism of the frequency shifts. Both gas phase collisions and wall collisions have been known to cause shifts in the magnetic resonance. For example in a gaseous mixture of optically pumped rubidium atoms and krypton atoms, which are nuclear spin polarized by spin exchange with the polarized Rb atoms, Schaefer et. al. observed a frequency shift in both the nuclear magnetic resonance (NMR) of Kr atoms and the EPR of Rb atoms [21]. The amount of shift is proportional to the polarization of the two atomic species. The frequency shift is due to the Fermi contact interaction between the s-electron of the alkali atom and the nucleus of the noble gas atom during the collision.

Collisions between optically pumped alkali atoms can also cause a frequency shift due to the spin exchange interaction [22]. Recently Dmitriev et. al. observed a shift in the EPR frequency of optically pumped Rb atoms due to collisions with optically

pumped Cs atoms [23].

Frequency shifts due to wall collisions have also been reported but only for the noble gas atoms ^{131}Xe, ^{201}Hg, ^{83}Kr and ^{21}Ne, which posses a quadrupole moment [24–28]. The shift is due to the quadrupole interaction between the quadrupole moment of the noble gas nucleus and the electric field gradient on the surface. The energy level shift due to quadrupole interaction is proportional to $3m_K^2 - K(K+1)$, where K is the nuclear spin of the noble gas atom and m_K is the magnetic quantum number of the spin K. Therefore, the quadrupole interaction causes a splitting of the nuclear magnetic resonance line. This quadrupolar splitting provides a clear signature of the frequency shift due to quadrupole interaction. This is in contrast to the shift due to Fermi contact interaction studied in this dissertation. The Zeeman energy level shift due to Fermi contact interaction is proportional to m_F, where m_F is the magnetic quantum number of the total angular momentum F. Therefore, it causes a shift but not splitting of the EPR lines, and it could be difficult to be distinguished from the shift due to an external magnetic field.

Spin polarized nuclei that have a quadrupole moment have been used in the search for anisotropy of inertial mass [2, 5–7]. According to Mach's principle, the inertia of a body is determined by the total distribution of matter in the universe. Since the mass distribution in our galaxy is anisotropic, the mass of a particle depends on the angle θ between the direction of its acceleration and the direction to the galactic center if we only consider the anisotropy distribution of matter in our galaxy. Thus the inertial

mass is a tensor. One can show that the simplest form of this orientation-dependent part of the mass can be written as $\Delta m P_2(\cos\theta)$ [5]. The energy shift associated with this anisotropic part of the mass is also proportional to $P_2(\cos\theta)$, and therefore the levels $m_K = \pm 3/2$ will have a different shift from the levels $m_K = \pm 1/2$. One of the most sensitive tests of this anisotropy of inertial mass was performed using the magnetic resonance of ^{21}Ne, which was nuclear spin polarized by spin exchange with optically pumped Rb atoms [2]. The choice of ^{21}Ne is due to its long relaxation time of 1.8 h, resulting in an exceedingly narrow linewidth. Due to its nuclear quadrupole moment, the quadrupole wall interaction causes the free precession of ^{21}Ne to exhibit beat, just like other noble gas atoms that have a nuclear quadrupole moment. However, a component at twice the Earth's sidereal frequency would suggest the existence of an orientation-dependent part of the mass. An upper limit of 10^{-28} of the binding energy per nucleon was set for the anisotropy of inertial mass.

In the first part of my dissertation, I describe a novel approach to study wall interactions. I measured an important parameter of the wall interaction, that is, the dwell time τ_s, on two of the most commonly used antirelaxation coatings, octadecyltrichlorosilane (OTS) and paraffin. The dwell time is the amount of time a polarized ^{87}Rb atom is adsorbed on the coating. In the second part, I describe the first observation of a large shift in the EPR frequency of gas phase rubidium atoms (^{87}Rb) due to collisions with nuclear spin polarized RbH-coated walls. The nuclei on the RbH salt surface are polarized by spin exchange with optically pumped Rb vapor.

The experimentally measured EPR frequency shift due to wall collisions also allowed us to calculate the average phase shift experienced by the polarized Rb atom while adsorbed on the salt surface.

1.2 Polarization of Solids

1.2.1 Dynamic Nuclear Polarization

The method of dynamic nuclear polarization (DNP) has long been used [29]. In my work I have used a novel method to polarize the surface of a salt, which is not through the usual method of electron saturation. In my study the nuclei of a salt are polarized through Fermi contact with polarized vapor, in which the surface is further polarized through spin exchange as will be discussed in a later section. The traditional method of polarizing the nuclei in a solid is through dynamic nuclear polarization (DNP), which can be understood through the Overhauser Effect. Overhauser proposed that the saturation of the electron paramagnetic resonance (EPR) can increase the nuclear polarization by a factor on the order of γ_e/γ_n (C.P. Slichter, 1996), where γ_e is the gyromagnetic ratio of the electron and γ_n is the gyromagnetic ratio of the nucleus. The following describes how the Overhauser Effect works. First, we derive the thermal nuclear polarization, $\langle P_z \rangle_{\text{thermal}}$. Consider the spin and nuclear interaction Hamiltonian:

$$H = \gamma_e \hbar B S_z - \gamma_n \hbar B K_z + A\hbar^2 S_z K_z \tag{1.1}$$

where B is the magnetic field, S_z is the z-component of the electron spin, K_z is the z-component of the nuclear spin, which we assume to have a spin quantum number $1/2$. γ_e and γ_n are the gyromagnetic ratios of the electron and nucleus respectively and the spin state of the electron and nucleus $|\ S_z\ K_z\rangle$ are

$$(1)\ |+-\rangle \tag{1.2}$$

$$(2)\ |--\rangle \tag{1.3}$$

$$(3)\ |++\rangle \tag{1.4}$$

$$(4)\ |-+\rangle \tag{1.5}$$

Using the Hamiltonian Eq.(1.1) we can write down the energy for each state:

$$|+-\rangle \rightarrow E_1 = \frac{1}{2}\gamma_e\hbar B + \frac{1}{2}\gamma_n\hbar B - \frac{1}{4}A \tag{1.6}$$

$$|--\rangle \rightarrow E_2 = -\frac{1}{2}\gamma_e\hbar B + \frac{1}{2}\gamma_n\hbar B + \frac{1}{4}A \tag{1.7}$$

$$|++\rangle \rightarrow E_3 = \frac{1}{2}\gamma_e\hbar B - \frac{1}{2}\gamma_n\hbar B + \frac{1}{4}A \tag{1.8}$$

$$|-+\rangle \rightarrow E_4 = -\frac{1}{2}\gamma_e\hbar B - \frac{1}{2}\gamma_n\hbar B - \frac{1}{4}A \tag{1.9}$$

With these definitions we can calculate the average thermal polarization of the nucleus $\langle K_z\rangle_{\text{thermal}}$ without EPR saturation. The percentage of the population in each of the

four states can be denoted as P_1, P_2, P_3 and P_4 and their sum should be equal to one, thus $P_1 + P_2 + P_3 + P_4 = 1$, therefore we can write the average polarization of the nucleus as

$$\langle K_z \rangle_{\text{thermal}} = -\frac{1}{2}P_1 - \frac{1}{2}P_2 + \frac{1}{2}P_3 + \frac{1}{2}P_4 \tag{1.10}$$

Using the Boltzmann distribution and keeping only the lowest order terms, the percentage of population in each state can be written as

$$P_1 = \frac{1}{4}e^{-E_1/kT} = \frac{1}{4}(1 - \frac{E_1}{kT}) \tag{1.11}$$

$$P_2 = \frac{1}{4}e^{-E_2/kT} = \frac{1}{4}(1 - \frac{E_2}{kT}) \tag{1.12}$$

$$P_3 = \frac{1}{4}e^{-E_3/kT} = \frac{1}{4}(1 - \frac{E_3}{kT}) \tag{1.13}$$

$$P_4 = \frac{1}{4}e^{-E_4/kT} = \frac{1}{4}(1 - \frac{E_4}{kT}) \tag{1.14}$$

where k is the Boltzmann constant. Thus, we find the average thermal polarization of the nucleus:

$$\langle K_z \rangle_{\text{thermal}} = \frac{1}{2}(P_3 + P_4 - P_1 - P_2) \tag{1.15}$$

$$\langle K_z \rangle_{\text{thermal}} = \frac{1}{8}((2 + \frac{\gamma_n \hbar B}{kT}) - (2 - \frac{\gamma_N \hbar B}{kT})) \tag{1.16}$$

$$\langle K_z \rangle_{\text{thermal}} = \frac{1}{4}\frac{\gamma_n \hbar B}{kT} \tag{1.17}$$

It is important to note that $\langle K_z \rangle_{\text{thermal}} \sim \gamma_n$, in which $\gamma_n \sim 1/m_p$ and $\gamma_e \sim 1/m_e$ where m_p is the mass of a proton and m_e is the mass of an electron. Since $m_p \gg m_e$, $\gamma_n < \gamma_e$. Without EPR saturation most of the atoms will tend to P$_2$, the lower energy state and so the populations in each state are not equal, P$_1 \neq$ P$_2$. In the case of EPR saturation we have P$_1 =$ P$_2$ as shown in Fig. 1.1 and we define

$$\frac{P_3}{P_1} = \frac{e^{-E_3/kT}}{e^{-E_1/kT}} = e^{-(E_3-E_1)/kT} \tag{1.18}$$

$$\frac{P_4}{P_1} = \frac{e^{-E_4/kT}}{e^{-E_1/kT}} = e^{-(E_4-E_1)/kT} \tag{1.19}$$

therefore

$$P_3 = e^{-(E_3-E_1)/kt} P_1 \tag{1.20}$$

$$P_4 = e^{-(E_4-E_1)/kt} P_1 \tag{1.21}$$

Now we can use the fact that P$_1$ + P$_2$ + P$_3$ + P$_4$ = 1, where P$_1 =$ P$_2$, to find the increase or decrease in the percentage of the population in each level from the thermal polarization:

$$P_1 \uparrow \frac{\gamma_e \hbar B}{16kT} \tag{1.22}$$

$$P_3 \uparrow \frac{\gamma_e \hbar B}{16kT} \tag{1.23}$$

$$P_4 \uparrow \frac{\gamma_e \hbar B}{16kT} \tag{1.24}$$

$$P_2 \downarrow \frac{3\gamma_e \hbar B}{16kT}. \tag{1.25}$$

The nuclear polarization due to EPR saturation is given as

For spin 1/2 nuclei

(1) | + - >

(3) | + + >

Saturation ($P_1 = P_2$)

(2) | - - >

(4) | - + >

FIG. 1.1. Energy levels of a spin 1/2 nucleus with percentage population increase or decrease in each level due to electron saturation given by Eq.(1.22), Eq.(1.23), Eq.(1.24) and Eq.(1.25).

$$\langle K_z \rangle_{\text{Overhauser}} = \frac{1}{8}(\frac{2\gamma_n \hbar B}{kT} + \frac{\gamma_e \hbar B}{kT}) \sim \frac{1}{8}\frac{\gamma_e \hbar B}{kT} \tag{1.26}$$

where we have neglected γ_n term since $\gamma_n \ll \gamma_e$. In order to understand how much the

nuclear polarization is increased due to electron saturation we can take the ratio of

the average nuclear polarization due to the Overhauser effect and the average thermal nuclear polarization:

$$\frac{\langle K_z \rangle_{\text{Overhauser}}}{\langle K_z \rangle_{\text{thermal}}} = \frac{\frac{1}{8}\frac{\gamma_e \hbar B}{kT}}{\frac{1}{4}\frac{\gamma_n \hbar B}{kT}} = \frac{1}{2}\frac{\gamma_e}{\gamma_n} \tag{1.27}$$

This ratio shows that the Overhasuer Effect increases the average nuclear polarization by 1,000 times, due to the fact that $\langle K_z \rangle_{\text{Overhauser}}$ is proportional to γ_e whereas $\langle K_z \rangle_{\text{thermal}}$ is proportional to γ_n.

1.2.2   Polarization Through Spin Exchange

It was recently discovered that alkali hydride (CsH) can be nuclear spin polarized by spin exchange with optically pumped Cs vapor [29]. Unlike the DNP method, which polarizes the nuclei in the bulk, in this new method the angular momentum is transferred to the salt at the surface, then propagates into the salt through spin diffusion. The polarization achieved in Ref. [29] is larger by a factor of four compared to that of the thermal polarization. The modest polarization enhancement is due to the following reasons. First, the nuclear polarization was measured using an NMR spectrometer and therefore required a high magnetic field ($\sim$ a few T). At such high magnetic fields, the efficiency of polarizing the nuclei of the gas phase Rb atoms through optical pumping is low because of the decoupling of the electron spin and the nuclear spin at high fields. Second, the spin exchange rate between a gas phase spin and a spin on the surface is proportional to $j(\Delta\omega) = 1/(1 + \tau_c^2 \Delta\omega^2)$, the Fourier

transform of the correlation function at frequency $\Delta\omega$, where $\Delta\omega$ is the difference between the Larmor frequencies of the two spins [18]. In low magnetic fields, $j(\Delta\omega)$ is practically equal to one for either the gas phase electron spin or nuclear spin. However, since the gyromagnetic ratios for electron and ^{87}Rb nuclei are respectively $\gamma_e = 2.8\,\mathrm{MHz/G}$ and $\gamma_{\mathrm{Rb}}(^{87}\mathrm{Rb})=1.394$ kHz/G, $j(\Delta\omega)$ at high fields can be orders of magnitude smaller than its value at low fields. Therefore, in our experiment, we expect the efficiency of polarizing the RbH surface to be much higher than the efficiency in polarizing the CsH surface in Ref. [29].

One can also make an educated rough estimate of the angular momentum flux into the RbH salt as follows. Due to the surface interaction of Rb atoms, there is a gradient of polarization near the cell surface, and consequently a flux of angular momentum from the gas phase into the surface [30, 31]. For simplicity we consider the one dimensional problem, $i.e.$ we assume the expectation value of the z component of the total angular momentum $\langle F_z \rangle$, where F_z is a conserved quantity in the present experiment, only depends on x. Note that the x-axis is the cell axis and is perpendicular to the front ($x = -L/2$) and back ($x = L/2$) surfaces of the cell, thus $\langle F_z \rangle$ is governed by the following equation

$$\frac{d\langle F_z \rangle}{dt} = R\left(1 - \langle F_z \rangle / F_0\right) + D\frac{d^2}{dx^2}\langle F_z \rangle. \qquad (1.28)$$

where $F_0 = I + 1/2 = 2$ is the value of $\langle F_z \rangle$ far away from the surface, with $I = 3/2$ being the nuclear spin of ^{87}Rb atoms, R the pumping rate (number of photons

absorbed per second) for an unpolarized ($\langle F_z \rangle = 0$) Rb vapor, and D the diffusion coefficient of Rb atoms in buffer gas (N_2). Again, for simplicity, we assume the expectation value $\langle F_z \rangle$ vanishes at the cell wall [31]. The steady state solution of Eq.(1.28) at the back surface is

$$\langle F_z \rangle (x) = F_0 \left[1 - \exp\left(-\sqrt{\frac{R}{D}} \, (x - L/2) \right) \right] . \qquad (1.29)$$

The angular momentum flux into the solid is given by

$$J_F = nD\frac{d}{dx}\langle F_z \rangle = nDF_0\sqrt{\frac{R}{D}} = nF_0\sqrt{RD} . \qquad (1.30)$$

where n is the Rb vapor density. Under typical experimental conditions, we have $n = 8 \times 10^{12}\,\text{cm}^{-3}$, $R \sim 10^4/\text{s}$, and $D = 30\,\text{cm}^2\text{s}^{-1}$. From Eq.(1.30) we have $J_F \sim 10^{16}\,\hbar\,\text{cm}^{-2}\,\text{s}^{-1}$. The lattice constant of RbH is 3.02 Å, and there are 10^{15} atoms on a unit surface area. Thus each atom on the RbH surface is hit by 10 units ($\hbar$) of angular momentum by the gas phase Rb atom per second.

1.3 Method for Measuring Polarization

Nuclear magnetic resonance is an established method to measure the polarization of a solid. It was used by Ishikawa et. al. to measure the enhancement factor discussed

in the previous section. As shown in section 1.1 the nuclear polarization is given by

$$\langle K_z \rangle_{\text{thermal}} = \frac{1}{4} \frac{\gamma_n \hbar B}{kT} \qquad (1.31)$$

One disadvantage of the NMR technique is that due to the smallness of γ_n, one needs to use a high magnetic field and low temperature.

The experiment described in this thesis opens up the possibility of studying surface NMR using gas phase EPR. Since the phase shift experienced by the gas phase rubidium atom while adsorbed on the surface is due to the interaction of the adsorbed Rb atom with the surface nucleus, our method is surface specific and the measured frequency shift only depends on surface polarization. This is in contrast to the traditional NMR method using an NMR spectrometer which measures the average bulk nuclear polarization. Since there is much interest in low dimensional magnetic materials, this method might be particularly interesting in those studies. As can be seen from equation Eq.(2.79) the surface polarization $\langle K_z \rangle$ can be obtained from the phase shift provided one has the information of the dwell time τ_s.

Chapter 2

Theory

The experiment described in this thesis consisted of measuring the EPR frequency shifts for σ^+ and σ^- pumping for a number of different cell lengths. From these measured EPR frequency shifts one can calculate surface interaction parameters such as average dwell time and average phase shift experienced by polarized Rb atoms while adsorbed on the wall. The calculations are based on a theory developed by Schaden et. al. [32]. Since both the experimental arrangement and the property of the walls are different in cells coated with antirelaxation coating and cells coated with RbH salt, the differential equations and boundary conditions that will be used to determine the wall interaction parameters are slightly different. I will discuss the two cases separately in the following.

2.1 Antirelaxation Walls

2.1.1 EPR Frequency Shift from Diffusion Equation

In the case of the antirelaxing surface, the Rb atoms are pumped with an evanescent pump beam. Thus, there is no contribution to the phase shift due to light. In fact, the light phase shift is treated as part of the phase shift due to the surface. Therefore, according to Ref. [32] the differential equation that describes this case is given as

$$\left(D\frac{d^2}{dx^2} - i\omega_o + \alpha_n \right) \psi_n(x) = 0, \tag{2.1}$$

with the boundary condition for $\psi_n(x)$ at the front $(x = -L/2)$ and back $(x = L/2)$ surfaces of the cell is given as

$$0 = \pm\frac{\partial}{\partial x}\psi_n(x) + \mu\psi_n(x) + \eta\frac{\partial^2}{\partial x^2}\psi_n(x) \mid_{x=\pm L/2}. \tag{2.2}$$

In Eq.(2.1) α_n is the eigenvalue corresponding the n-th longitudinal mode of $\psi_n(x)$ and ω_0 is the EPR frequency of the Rb atom in the bulk. The coefficients μ and η in the boundary condition are given as the following

$$\mu = \frac{3(\xi_s \pm i\delta\phi_s)}{4\lambda} \tag{2.3}$$

$$\eta = \frac{\tau_s\bar{v}}{4}, \tag{2.4}$$

where ξ_s is the average relaxation probability for a polarized [87]Rb atom during the average dwell time τ_s on the cell wall, $\lambda = 3.0 \times 10^{-3}$ cm is the mean free path of [87]Rb atoms in the N_2 gas, and $\bar{v} = \sqrt{8kT/\pi m} = 3.0 \times 10^4$ cm/s is the mean speed of [87]Rb atoms [34]. The $\pm$ sign in front of $\delta\phi_s$ refers to the $\sigma^{\pm}$ pumping.

The three terms on the right hand side of the boundary condition can be written in dimensionless quantities as 1, μL, and η/L. To estimate the magnitude of these terms relative to one another we must estimate the parameters ξ_s, τ_s, and $\delta\phi_s$. It has been found in an OTS-coated cell that $\xi_s = 1.3 \times 10^{-3}$ [20]. Moreover, the dwell time τ_s of OTS-coated cells has been found to be ~ 1.0 μs [30, 35]. Therefore, $\mu L = 0.03$ and $\eta/L = 0.1$, and the last two terms in the boundary condition Eq.(2.2) are not negligible and cannot be ignored.

The solutions to Eq.(2.1) and its boundary condition Eq.(2.2) are proportional to either $\cos(k_n x)$ or $\sin(k_n x)$. This is because both the differential equation and boundary condition have parity symmetry, thus the solution must also have parity symmetry. Only the lowest mode contributes to the signal, as the higher modes are too broad [36]. The wave number $k_0 = 2u_0/L$ is determined by the boundary condition.

$$\tan u_o = \frac{L\mu}{2u_o} - \frac{2\eta}{L}u_o \qquad (2.5)$$

Because $u_0 \ll 1$, we can expand $\tan u_0$ and keep only the first term. Eq.(2.5) then becomes

$$u_o = \frac{L\mu}{2u_o} - \frac{2\eta}{L}u_o \ , \qquad (2.6)$$

from which we have

$$2u_o^2 = \frac{L\mu}{1 + \dfrac{2\eta}{L}} \tag{2.7}$$

The eigenvalue α_0 is given by

$$\alpha_0 = i\omega_0 + D\frac{4u_o^2}{L^2} = i\omega_0 + \frac{2D}{L^2}\frac{L\mu}{1 + \dfrac{2\eta}{L}} = i\omega_0 + \frac{\xi_s \pm i\delta\phi_s}{\dfrac{2L}{\bar{v}} + \tau_s} \tag{2.8}$$

where we have used $D = \lambda\bar{v}/3$. Therefore the EPR frequency in the presence of wall collisions, which is the imaginary part of the eigenvalue α_0 of Eq.(2.8), is given by

$$\omega^{(\pm)} = \omega_0 \pm \frac{\delta\phi_s}{\dfrac{2L}{\bar{v}} + \tau_s} . \tag{2.9}$$

where $\pm$ refers to $\sigma^\pm$ pumping. We now define $\Delta = \omega^{(-)} - \omega^{(+)}$, thus from Eq.(2.9) we have

$$\Delta = -\frac{2\delta\phi_s}{\dfrac{2L}{\bar{v}} + \tau_s} , \tag{2.10}$$

Eq.(2.10) can be written as

$$\frac{2L}{\bar{v}} = -2\delta\phi_s\frac{1}{\Delta} - \tau_s \tag{2.11}$$

Therefore we see that there is a linear relationship between the cell length L and $1/\Delta$.

2.1.2 EPR Frequency Shift from the Gas Kinetic Theory

Alternatively, Eq.(2.11) can also be derived using the gas kinetic theory. Consider the diffusion path of a spin polarized Rb atom from the time it is polarized to the time it relaxes. The path can be divided into N segments as depicted in Fig. 2.1 , with each segment corresponding to the path between two consecutive wall collisions. The average EPR frequency shift for the Rb atom before it relaxes is given by

$$\omega^{(\pm)} - \omega_o = \frac{\displaystyle\sum_{i=1}^{N} \delta\phi_{s,i} + \sum_{i=1}^{N} \delta\phi_{\text{light},i}^{(\pm)}}{\displaystyle\sum_{i=1}^{N} \tau_{s,i} + \sum_{i=1}^{N} \tau_{b,i}} \tag{2.12}$$

which becomes, upon dividing the numerator and denominator of Eq.(2.12) by N,

$$\overline{\omega^{(\pm)}} - \omega_0 = \pm \frac{\overline{\delta\phi_s} + \overline{\delta\phi_{\text{light}}}}{\overline{\tau_s} + \overline{\tau_b}}, \tag{2.13}$$

where the bar indicates the average over the N segments. If N is sufficiently large, as is the case for good coatings such as OTS and paraffin, the distribution of the frequency shifts $\omega^{(\pm)} - \omega_o$ for all the Rb atoms will be sufficiently narrow to allow for a well-defined ensemble average frequency shift given by

$$\omega^{(\pm)} = \omega_o \pm \frac{\delta\phi_{\text{s}} + \delta\phi_{\text{light}}}{\tau_{\text{s}} + \tau_{\text{b}}} \tag{2.14}$$

In Eq.(2.14) $\delta\phi_{\text{light}}$ is the average phase shift of the Rb atom during its interaction with the evanescent $\sigma^{(\pm)}$ pump beam due to the light shift. Using $\Delta = \omega^{(-)} - \omega^{(+)}$ we have

$$\Delta = \frac{-2(\delta\phi_s + \delta\phi_{\text{light}})}{\tau_s + \tau_b} = \frac{-2(\delta\phi_s + \delta\phi_{\text{light}})}{\tau_s + 2L/\bar{v}} \tag{2.15}$$

Here we have used $\tau_b = 2L/\bar{v}$ where $\bar{v} = \sqrt{8kT/\pi m} = 3.0 \times 10^4$ cm/s is the mean speed of ^{87}Rb atoms. The time that a Rb atom spends in the gas phase before two consecutive collisions is purely a gas kinetic quantity, independent of the spin state of the Rb atom. Therefore, the expression for τ_b can be derived from the well known gas kinetic formula $An\bar{v}/4$ for the total number of collisions per second of Rb atoms on the front surface of area A. Thus the total number of collisions per second of Rb atoms on the front surface or back surface is $n\bar{v}A/2$, which can be written as $\bar{v}N/2L$, where N is the total number of Rb atoms in the vapor. Accordingly, the rate of a single atom hitting the front or back surface is $\bar{v}/2L$, the inverse of which yields the average time τ_b that a Rb atom spends in the bulk between two consecutive wall collisions: $\tau_b = 2L/\bar{v} = \sqrt{3\pi/2}L/v_{rms}$.

In the case of the antirelaxation coating we have used an evanescent pump beam and thus, the phase shift due to the light is treated as a phase shift due to the surface. We define $\delta\phi = \delta\phi_s - \delta\phi_{\text{light}}$ and Eq.(2.15) can be written as

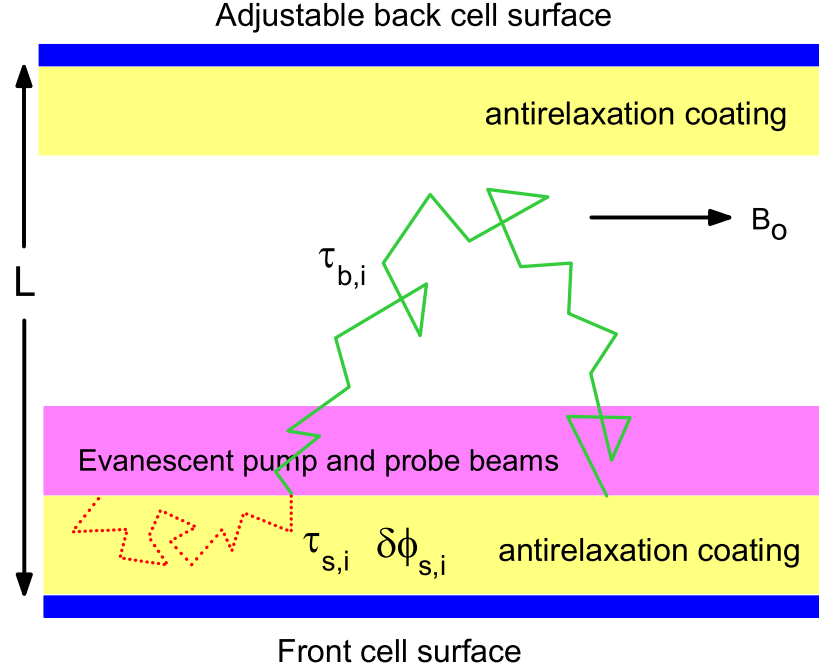$$\frac{2L}{\bar{v}} = -2\delta\phi\frac{1}{\Delta} - \tau_s \tag{2.16}$$

FIG. 2.1. A representative i-th segment of the diffusion path of a Rb atom between two consecutive wall collisions. The part of the segment in coating (in red) is associated with the surface induced phase shift $\delta\phi_{s,i}$ and the dwell time $\tau_{s,i}$ and the part of the segment in the bulk (in green) is associated with the phase shift $\delta\phi_{light,i}^{(\pm)}$ due to the light shift in the evanescent pump beam and a time $\tau_{b,i}$ which is the time the Rb atom spends in the bulk between two consecutive wall collisions. B_0 is the uniform magnetic field along the z direction, and B_{eff} is the effective magnetic field due to the light shift of the pump beam. The figure is not drawn to scale.

which is the same result found by Eq.(2.11) in the previous section.

2.2   Polarized Walls

As described in section 1.2.2 the surface of the rubidium hydride salt can be polarized through spin exchange with polarized rubidium vapor. This implies that there is a significant amount of angular momentum flux into the surface, which accounts for the much larger wall relaxation rate for the Rb vapor. Therefore, in the RbH coated cell the signal is much worse than in cells coated with antirelaxation coating. Instead of using an evanescent wave to pump the vapor, to improve the signal to noise ratio in RbH-coated cells the pump beam illuminates the entire cell.

The differential equation for the polarized wall is given by

$$\left(D\frac{d^2}{dx^2} - i\omega_o \mp i\delta\omega_{\text{light}} + \alpha_n \right) \psi_n(x) = 0. \tag{2.17}$$

where $\pm$ again refers to σ^+ and σ^- pumping. Because the pump beam uniformly illuminates the entire cell, the light shift due to the pump beam is equivalent to a uniform magnetic field applied to the cell, which is taken into account by the term $\mp i\delta\omega_{\text{light}}$ in Eq.(2.17). The boundary conditions for Eq.(2.17) are

$$0 = \pm\frac{\partial}{\partial x}\psi_n(x) + \mu\psi_n(x) + \eta\frac{\partial^2}{\partial x^2}\psi_n(x) \mid_{x=\pm L/2} .$$

We can again use the dimensionless quantities 1, μL, and η/L to estimate the relative magnitude of the three terms on the right hand side of the boundary condition.

Recalling the definitions of μ and η in Eq.(2.3) and Eq.(2.4) respectively, we would like to estimate the parameters ξ_s, $\delta\phi_s$ and τ_s. First off, the relaxation probability ξ_s can be found using the linewidth of the EPR curve, which, as discussed in the previous section increases with decreasing cell length L because the wall collision rate increases with decreasing L. For $L = 0.15$ cm, the linewidths in the absence of rf broadening is 2.37 kHz (see section 4.2.2). This linewidth is contributed by the wall relaxation and the gas phase relaxation. The latter should be the same as in OTS-coated cells, which was found to be 0.75 kHz [33]. Therefore the linewidths due to wall relaxation is about 1.6 kHz, from which one obtains the relaxation rate due to wall collisions as $2\pi \times$ 1.6 kHz $= 1.0 \times 10^4$ s^{-1}. In order to make an estimation of ξ_s we need to know the rate of wall collisions for ^{87}Rb atoms. The rate of a single ^{87}Rb atom hitting the front or back surface is $\bar{v}/2L$. For a cell thickness of 1.5 mm, the wall collision rate is $\bar{v}/2L = 1.0 \times 10^5$ s^{-1}. Therefore the average relaxation probability for a polarized Rb atom during a wall collision is $\xi_s = 1.0 \times 10^4$ s$^{-1}/10^5$ s$^{-1} = 0.1$, which is reasonable compared to that of an OTS-coated cell where $\xi_s = 1.3 \times 10^{-3}$ [20]. Even though τ_s for Rb atoms on the RbH surface has not been reported to our knowledge, it is reasonable to assume that τ_s for Rb atoms on the rigid RbH crystal is less than τ_s of the Rb on paraffin or OTS-surfaces which was found to be of the order μs. Since $\mu L \sim 5$ and $\eta/L \sim 5 \times 10^{-4}$, we find that the second derivative term in the boundary condition is insignificant in the present experiment and will be

omitted. The boundary condition Eq.(2.2) then becomes

$$0 = \pm \frac{\partial}{\partial x} \psi_n(x) + \mu \psi_n(x) \mid_{x=\pm L/2} . \tag{2.18}$$

Boundary condition Eq.(2.18) was used in previous studies of wall interactions of spin polarized atoms [37, 38]. Just as in case 1, Eq.(2.17) and its boundary condition Eq.(2.18) have parity symmetry, and so its solutions are also eigenfunctions of parity, and proportional to either $\cos(k_n x)$ or $\sin(k_n x)$. Since the pumping beam is uniform throughout the cell, the contributions from all the modes except the lowest one are negligibly small. Therefore we need to only consider the lowest mode, which is proportional to $\cos(k_0 x)$ and corresponds to eigenvalues $\alpha_o = i\omega_o + i\delta\omega_{light} + Dk_o^2$ for $\sigma^{\pm}$ pumping. The EPR frequency, which is the imaginary part of the eigenvalue [32], is given as

$$\omega^{(\pm)} = \omega_0 \pm \delta\omega_{\text{light}} \pm \delta\omega_s \tag{2.19}$$

The EPR frequency shift $\delta\omega_s$ due to wall collisions is given by

$$\delta\omega_s = \text{Im } Dk_0^2 \tag{2.20}$$

We use $\Delta = \omega^{(-)} - \omega^{(+)}$ and Eq.(2.19) to find

$$\delta\omega_s = \frac{-\Delta - 2\delta\omega_{\text{light}}}{2} \tag{2.21}$$

Now, substituting $\cos(k_o\,x)$ into the boundary conditions Eq.(2.18), we find the wave number $k_o = 2u_o\,/\,L$ to be the solution of the following equation:

$$u_o \tan(u_o) = \frac{L\mu}{2} \qquad 0 < \text{Re } u_o < \pi/2 \tag{2.22}$$

with

$$u_o \tan(u_o) = \frac{3L\xi_s}{8\lambda} + i\frac{3L\delta\phi_s}{8\lambda} \tag{2.23}$$

Because of the substantial phase shift $\delta\phi_s$ on the RbH walls the solution to Eq.(2.22) is a complex number. We therefore write $u_o = u_o' + iu_o''$. The EPR frequency shift due to wall collisions which is given by Eq.(2.20) can be written as

$$\delta\omega_s = \frac{8D}{L^2}u_o' u_o''. \tag{2.24}$$

$$\frac{8D}{L^2}u_o' u_o'' = \text{Im}Dk_0^2 = \delta\omega_s \tag{2.25}$$

We separate the real and imaginary parts in the boundary condition, which then becomes

$$\frac{u_o'\tan u_o'\,\text{sech}^2 u_o'' - u_o''\tanh u_o''\sec^2 u_o'}{1 + \tan^2 u_o'\tanh^2 u_o''} = \frac{3L\xi_s}{8\lambda}, \tag{2.26}$$

and

$$\frac{u_o''\tan u_o'\,\text{sech}^2 u_o'' + u_o'\tanh u_o''\sec^2 u_o'}{1 + \tan^2 u_o'\tanh^2 u_o''} = \frac{3L\delta\phi_s}{8\lambda}. \tag{2.27}$$

Our goal is to calculate u_0' and u_0'' from Eq.(2.24) and Eq.(2.26) and we can then calculate the phase shift $\delta\phi_s$ in Eq.(2.27).

2.3   Zeeman Levels and Coherences

2.3.1   Zeeman Splitting and Breit-Rabi Formula

The end transitions between the Zeeman levels ($m_f = 2 \to m_f = 1$ and $m_f = -2 \to m_f = -1$) are not equal. In order to make sure that the observed EPR frequency difference for σ^+ and σ^- pumping is not due to the difference between the frequencies of the end transitions, we need to estimate the difference between the end transitions for the holding field used in the present experiment.

The Zeeman energy level splitting for the $F = 2$ ground state of ^{87}Rb is given by the Breit-Rabi formula [39]

$$\Delta E(F, M) = -\frac{h\Delta\nu}{2I(I+1)} - g_I'\mu_B BM \pm \frac{1}{2}h\Delta\nu \times (1 + \frac{4M}{2I+1}x + x^2)^{1/2} \qquad (2.28)$$

where the hyperfine structure frequency is given as $\Delta\nu =$6.834681 $\times 10^9$ Hz/G, $g_I' = g_I\mu_n/\mu_B$ and the nuclear spin I is 3/2. Furthermore x is defined as

$$x = \frac{(g_J + g_I')\mu_B B}{h\Delta\nu} \qquad (2.29)$$

where μ_B is the Bohr magneton, g_J is the Lande factor and g_I is the nuclear g-

factor. To calculate x in Eq.(2.29) the following values are used: $g_J\,\mu_B/h = 2.8\times10^6$ Hz/G and $g_I\mu_B/h = 1398$ Hz/G. $\Delta E/h$ was calculated for each magnetic sublevel ($m_f = -2,-1,0,1,2$) and plotted versus the magnetic field, B. From Fig. 2.2 one can see the energy splitting between neighboring magnetic sublevels ($m_f = 1 \rightarrow 2, m_f = 1 \rightarrow 0, m_f = 0 \rightarrow -1, m_f = -1 \rightarrow -2$). At low fields the frequencies of the end transitions are approximately equal however at high fields the frequency at end transitions can be very different. Using the Breit-Rabi formula, the difference between the frequencies of the end transitions for the field used in our experiment ($\sim$ 0.1 G) was found to be about 4 Hz and therefore can be neglected. Furthermore, the different end transition frequencies lead to $\omega^{(-)} > \omega^{(+)}$, opposite to frequency shift due to the wall collisions.

We also want to point out that the gyromagnetic ratio for the $F = 1$ and $F = 2$ levels are equal in magnitude but opposite in sign. This can be seen as follows.

We note that $\vec{\mu}_F = \vec{\mu}_S + \vec{\mu}_I$, where the magnetic moments for both the spin angular momentum and the nuclear angular momentum are proportional to the inverse of the respective masses. The mass of the nucleus is three orders of magnitude larger than that of the electron, and therefore $\vec{\mu}_I$ can be neglected. Thus we have $\vec{\mu}_F = \vec{\mu}_S = \gamma_S\vec{S}$. We need to write $\vec{S}$ in terms of $\vec{F}$ because $\vec{F}$ is conserved. We have

$$\vec{S} = \frac{\vec{S}\cdot\vec{F}}{\vec{F}^2}\vec{F} \qquad (2.30)$$

Now using $\vec{F}\cdot\vec{S} = (\vec{F}^2 + \vec{S}^2 - \vec{I}^2)/2$ and substituting into $\vec{\mu}_F = \gamma_S(\vec{S}\cdot\vec{F}/\vec{F}^2)\vec{F}$ we

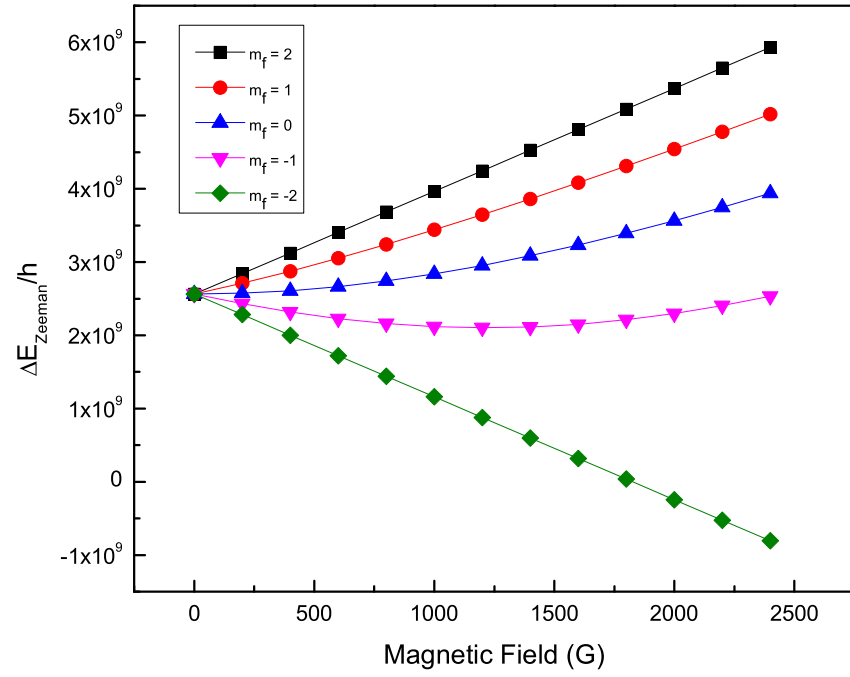FIG. 2.2. The dependence of the Zeeman energy splitting between the m_f levels in the ground state of ^{87}Rb on magnetic field.

get

$$\vec{\mu}_F = \gamma_S \frac{F^2 + S^2 - I^2}{2F^2} \vec{F} \tag{2.31}$$

For $F = I + 1/2$ level, we have

$$\vec{\mu}_F = \gamma_S \frac{(I + 1/2)(I + 3/2) + 1/2 \cdot 3/2 - I(I + 1)}{2(I + 1/2)(I + 3/2)} \vec{F} \tag{2.32}$$

or

$$\vec{\mu}_F = \gamma_S \frac{1}{2I + 1} \vec{F} \tag{2.33}$$

For $F = I - 1/2$, we have

$$\vec{\mu}_S = \gamma_S \frac{(I - 1/2)(I + 1/2) + 1/2 \cdot 3/2 - I(I + 1)}{2(I - 1/2)(I + 1/2)} \vec{F} \tag{2.34}$$

or

$$\vec{\mu}_S = -\gamma_S \frac{1}{2I + 1} \vec{F} \tag{2.35}$$

Therefore we see that the Larmor frequency of the Rb atom in $F = 1$ and $F = 2$ levels are equal in magnitude but opposite in sign.

2.3.2 Zeeman Coherences and the Calculation of the Faraday Rotation Angle

In order to understand the basic physics behind the signal measured in the experiment, we need to have a clear understanding of the Faraday rotation angle which determines the signal as discussed in section 3.1.2. Consider a Rb atom in the presence of a static holding field B_0 along the z-axis and an oscillating magnetic field $2B_1 \cos \omega t$ along the y-axis. We will look at this problem using both a classical description and a quantum mechanical description.

(i) *Classical Description*

The equation of motion of $\boldsymbol{\mu}$, the magnetic moment associated with the spin $\boldsymbol{S}$ of the Rb atom, is

$$\frac{d\boldsymbol{\mu}}{dt} = \boldsymbol{\mu} \times \gamma(B_0 \ \hat{\boldsymbol{z}} + 2B_1 \cos \omega t \ \hat{\boldsymbol{y}}) \tag{2.36}$$

where $\boldsymbol{\mu} = \gamma \boldsymbol{S}$, in which γ is the gyromagnetic ratio. The oscillating magnetic field $2B_1 \cos \omega t \ \hat{\boldsymbol{y}}$ can be viewed as the sum of a clockwise rotating and a counterclockwise rotating field:

$$2B_1 \cos \omega t \ \hat{\boldsymbol{y}} = (B_1 \cos \omega t \ \hat{\boldsymbol{y}} + B_1 \sin \omega t \ \hat{\boldsymbol{x}}) + (B_1 \cos \omega t \ \hat{\boldsymbol{y}} - B_1 \sin \omega t \ \hat{\boldsymbol{x}}) \ . \tag{2.37}$$

From classical mechanics we know that the equation of motion of $\boldsymbol{\mu}$ in a coordinate system rotating with a positive angular velocity ω (counterclockwise) around the

z-axis is given by

$$\frac{\delta\boldsymbol{\mu}}{\delta t} = \boldsymbol{\mu} \times \left((\gamma B_0 + \omega)\, \boldsymbol{z} + \gamma B_1\, \boldsymbol{y}\right) \tag{2.38}$$
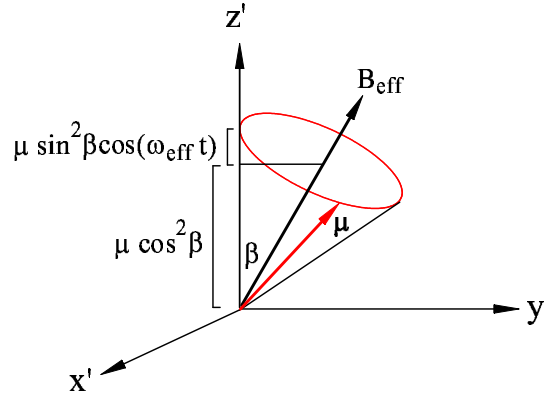

FIG. 2.3. Motion of the magnetic moment $\boldsymbol{\mu}$ in the rotating coordinate system.

Therefore in this rotating coordinate system the counterclockwise rotating field $B_1 \cos\omega t\; \boldsymbol{y} - B_1 \sin\omega t\; \boldsymbol{x}$ becomes a static field of amplitude B_1 along the y'-axis of the rotating coordinate system [40]. Since the clockwise rotating component of the oscillating field has negligible effect in the first order approximation (the Bloch-Siegert effect [41]) it can be omitted here. Because the axis of the rotating coordinate system is along the direction of $B_0 \hat{\boldsymbol{z}}$, $B_0 \hat{\boldsymbol{z}}$ will also be static in the rotating coordinate system.

Therefore in the rotating coordinate system, the magnetic moment $\boldsymbol{\mu}$ precesses around

a static effective magnetic field (see Fig. 2.3),

$$\boldsymbol{B}_{\text{eff}} = \boldsymbol{z} \left(B_0 + \frac{\omega}{\gamma} \right) + B_1 \, \boldsymbol{y} \; . \tag{2.39}$$

The angle β between $\boldsymbol{B}_{\text{eff}}$ and the z-axis is determined by

$$\tan \beta = \frac{B_1}{B_0 + \omega/\gamma} = \frac{\omega_1}{\omega_0 - \omega} \; , \tag{2.40}$$

where we have defined $\omega_0 = -\gamma B_0$ and $\omega_1 = -\gamma B_1$. If the resonance condition $\omega = \omega_0$

is satisfied, one sees from Eq.(2.39) that the effective field is $B_1 \, \boldsymbol{y}$. Therefore, if the

spin is initially along the z-axis, it will precess in the zx-plane, becoming periodically

parallel and anti-parallel to the z direction.

The Faraday rotation angle $\Delta\theta$ is given by

$$\Delta\theta = \pi \frac{n'_+ - n'_-}{\lambda} l \tag{2.41}$$

where n'_+ (n'_-) is the real part of the index of refraction of the Rb vapor for the σ^+

(σ^-) polarized component of the s-polarized probe beam, and l is the path length of

the probe beam. We note that $n'_+ - n'_-$ is proportional to the polarization along the

z-axis, which is given by (see Fig. 2.3)

$$\mu \cos^2 \beta + \mu \sin^2 \beta \cos(\omega_{\text{eff}} t) , \tag{2.42}$$

where $\omega_{\text{eff}} = -\gamma B_{\text{eff}}$ is the Larmor frequency around the effective field B_{eff}. Therefore the time dependence of the Faraday rotation angle can be written as

$$\mu - 2\mu \sin^2 \beta \sin^2 \left(\frac{\omega_{\text{eff}} t}{2} \right) . \tag{2.43}$$

According to section 3.1.2, the Faraday rotation signal is proportional to the Faraday rotation angle, and the lock-in output signal is proportional to the difference between the Faraday rotation signal when the oscillating magnetic field is on, which is given by Eq.(2.43), and that when the oscillating magnetic field is off, which is μ because $\beta = 0$ when the oscillating magnetic field is turned off. Therefore the lock-in signal S is given by

$$S \sim 2\mu \sin^2 \beta \sin^2(\omega_{\text{eff}} t/2) . \tag{2.44}$$

Since the chopping frequency of the oscillating field $\Omega \ll \omega_{\text{eff}}$, we can take the average value of the right hand side of Eq.(2.44), which then becomes

$$S \sim \sin^2 \beta = \frac{\omega_1^2}{(\omega_0 - \omega)^2 + \omega_1^2} . \tag{2.45}$$

The lock-in output signal has a Lorentzian shape, and increases with the rf field

amplitude. We also note that linewidth increases as well.

(ii) *Quantum Mechanical Description*

In the quantum mechanical description, the holding field creates Zeeman splitting. Due to the oscillating magnetic field, the Hamiltonian acquires off-diagonal elements and produces coherences between the Zeeman levels. We can neglect the nuclear spin of the Rb atom, for simplicity, and thus have a standard two-level system. We will also neglect the relaxation of the Rb atoms. In the basis $|\pm\rangle = |S_z = -1/2\rangle$, the Hamiltonian in the presence of a static magnetic field along the z-axis and a counterclockwise rotating field in the xy-plane is

$$H = -\hbar\gamma B_0 S_z - \hbar\gamma B_1(\cos\omega t\, S_y - \sin\omega t\, S_x) \tag{2.46}$$

One can show that

$$\cos\omega t\, S_y - \sin\omega t\, S_x = \exp(-i\omega t\, S_z)S_y\exp(i\omega t\, S_z) \tag{2.47}$$

Therefore we can write

$$H = \exp(-i\omega\, tS_z)(-\hbar\gamma B_0 S_z - \hbar B_1 S_y)\exp(i\omega\, tS_z) \tag{2.48}$$

Eq.(2.48) can be written as

$$H = \exp(-i\omega\, t S_z)(\hbar\omega_0 S_z + \hbar\omega_1 S_y)\exp(i\omega\, t S_z) \tag{2.49}$$

We note that $\exp(i\omega\, t S_z)$ is the rotation operator, which rotates the coordinates system xyz around the z-axis into the coordinate system $x'y'z'$ by an angle ωt. Thus, the coordinate system $x'y'z'$ can be regarded as rotating around the z-axis at an angular velocity ω. We now apply this rotation operator to the state ket $|\psi(t)\rangle$:

$$|\tilde{\psi}(t)\rangle = \exp(i\omega t\, S_z)|\psi(t)\rangle \tag{2.50}$$

Using Eq.(2.48) and Eq.(2.50) the Schrodinger equation

$$i\hbar\frac{\partial}{\partial t}|\psi(t)\rangle = H|\psi(t)\rangle\,, \tag{2.51}$$

can be written in the rotating coordinate system as

$$i\hbar\frac{\partial|\tilde{\psi}(t)\rangle}{\partial t} = \tilde{H}|\tilde{\psi}(t)\rangle\,, \tag{2.52}$$

where the Hamiltonian $\tilde{H}$ is

$$\tilde{H} = \hbar\left((\omega_0 - \omega)S_z + \omega_1 S_y\right)\,. \tag{2.53}$$

To solve Eq.(2.52) we first need to find the eigenkets of $\tilde{H}$. One can show that the eigenvalues of $\tilde{H}$ are

$$\tilde{E}_{\pm} = \pm\frac{\hbar}{2}\sqrt{(\omega_0 - \omega)^2 + \omega_1^2} \tag{2.54}$$

and the corresponding eigenkets are [42]

$$\widetilde{|+\rangle} = \cos\frac{\beta}{2}\,|+\rangle + \sin\frac{\beta}{2}\,|-\rangle, \tag{2.55}$$

$$\widetilde{|-\rangle} = -\sin\frac{\beta}{2}\,|+\rangle + \cos\frac{\beta}{2}\,|-\rangle, \tag{2.56}$$

where the angle β is defined in Eq.(2.40). The inverse of Eq.(2.55) and Eq.(2.56) are

$$|+\rangle = \cos\frac{\beta}{2}\,\widetilde{|+\rangle} - \sin\frac{\beta}{2}\,\widetilde{|-\rangle}, \tag{2.57}$$

$$|-\rangle = \sin\frac{\beta}{2}\,\widetilde{|+\rangle} + \cos\frac{\beta}{2}\,\widetilde{|-\rangle}. \tag{2.58}$$

Suppose at time $t = 0$ the spin is in the $|+\rangle$ state: $|\psi(0)\rangle = |+\rangle$. We expand this state in terms of the eigenstates of $\tilde{H}$:

$$|\psi(0)\rangle = \cos\frac{\beta}{2}\,\widetilde{|+\rangle} - \sin\frac{\beta}{2}\,\widetilde{|-\rangle}. \tag{2.59}$$

Then $|\psi(t)\rangle$ is given by:

$$|\psi(t)\rangle = \exp\left(\frac{i}{\hbar}\tilde{H}\,t\right)|\psi(0)\rangle \tag{2.60}$$

Using Eq.(2.59) we have from Eq.(2.60)

$$|\psi(t)\rangle = \cos\frac{\beta}{2}\exp\left(-\frac{i}{\hbar}\tilde{E}_+t\right)\widetilde{|+\rangle} - \sin\frac{\beta}{2}\exp\left(-\frac{i}{\hbar}\tilde{E}_-t\right)\widetilde{|-\rangle}, \tag{2.61}$$

or

$$|\psi(t)\rangle == \begin{pmatrix} \cos^2\frac{\beta}{2}\exp\left(-\frac{i}{\hbar}\tilde{E}_+t\right) + \sin^2\frac{\beta}{2}\exp\left(-\frac{i}{\hbar}\tilde{E}_-t\right) \\ \cos\frac{\beta}{2}\sin\frac{\beta}{2}\exp\left(-\frac{i}{\hbar}\tilde{E}_+t\right) - \sin\frac{\beta}{2}\cos\frac{\beta}{2}\exp\left(-\frac{i}{\hbar}\tilde{E}_-t\right) \end{pmatrix}. \tag{2.62}$$

The Faraday rotation angle is proportional to the difference between the populations in $|+\rangle$ and $|-\rangle$ states [43], and therefore is proportional

$$\left|\cos^2\frac{\beta}{2}\exp\left(-\frac{i}{\hbar}\tilde{E}_+t\right) + \sin^2\frac{\beta}{2}\exp\left(-\frac{i}{\hbar}\tilde{E}_-t\right)\right|^2 -$$
$$\left|\cos\frac{\beta}{2}\sin\frac{\beta}{2}\exp\left(-\frac{i}{\hbar}\tilde{E}_+t\right) - \sin\frac{\beta}{2}\cos\frac{\beta}{2}\exp\left(-\frac{i}{\hbar}\tilde{E}_-t\right)\right|^2 \tag{2.63}$$

or

$$1 - 2\sin^2\beta\sin^2\left(\frac{\tilde{E}_+ - \tilde{E}_-}{2\hbar}t\right) \tag{2.64}$$

Again, the lock-in output is proportional to the difference between the Faraday rotation signal when the oscillating magnetic field is on, which is given by Eq.(2.64), and that when the oscillating magnetic field is off, which is 1. The latter can be seen from Eq.(2.64) by letting $\omega_1 = 0$. The input of the lock-in can be seen in Fig.2.4.

Therefore the lock-in signal S is given by

$$S \sim 2\sin^2\beta\sin^2\left(\frac{\tilde{E}_+ - \tilde{E}_-}{2\hbar}t\right) \ . \tag{2.65}$$
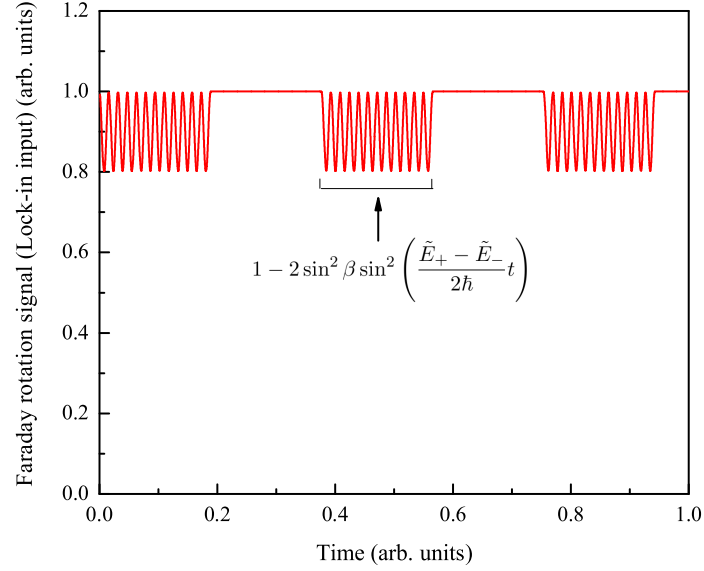

FIG. 2.4. Schematic of the lock-in input (the Faraday rotation signal).

Since the chopping frequency of the oscillating field $\Omega \ll (\tilde{E}_+ - \tilde{E}_-)/2\hbar$, we can

take the average value of the right hand side of Eq.(2.65), which then becomes

$$S \sim \sin^2 \beta = \frac{\omega_1^2}{(\omega_0 - \omega)^2 + \omega_1^2} \; , \qquad (2.66)$$

in agreement with the classical description Eq.(2.45).

2.4   Fermi Contact Interaction

2.4.1   Surface Interaction

Bouchiat and Brossel made a thorough study of the relaxation of Rb atoms adsorbed on the paraffin surface [18]. They found that two interactions are responsible for the disorientation of the Rb atoms. One is the dipole-dipole interaction between the spin S of the s-electron of the Rb atom and the nuclear spin K of the proton on the paraffin surface, where the carbon spin is zero. The other is the spin-orbit interaction of the s-electron at the carbon atom site, as the spin-orbit interaction at the proton site is much smaller due to the fact that the spin-orbit interaction increases rapidly with the atomic number Z of the nucleus [44]. We will assume that on the RbH surface the s-electron of the adsorbed ^{87}Rb atom experiences the same two types of interactions. The spin-orbit interaction is mainly contributed by the Rb ions on the RbH surface for the same reason that the spin-orbit interaction is mainly determined by the carbon atoms on the paraffin surface. The spin-orbit interaction relaxes the

spin angular momentum of the ^{87}Rb atoms, and therefore does not contribute to the nuclear polarization of the RbH surface or the frequency shift of the gas phase ^{87}Rb atoms. The dipole-dipole interaction between the s-electron of the adsorbed ^{87}Rb and the nucleus on the RbH surface consists of the scalar (Fermi contact) and tensorial parts. As was first shown by Herman, the electron exchange effect enhances the Fermi contact interaction by as much as five orders of magnitude, making the tensorial part of the dipole-dipole interaction unimportant [45] (see section 2.4.3). Therefore, the tensorial part of the dipole-dipole interaction will be neglected in our discussion and we will focus on the Fermi contact interaction.

2.4.2   Hamiltonian

The Hamiltonian of the Fermi contact interaction between the s-electron of the adsorbed ^{87}Rb atom and the nucleus on the salt is

$$H = \alpha \mathbf{S} \cdot \mathbf{K} \tag{2.67}$$

where $\boldsymbol{S}$ is the spin (in units of $\hbar$) of the s-electron of the adsorbed ^{87}Rb atom, $\boldsymbol{K}$ is the nuclear spin (in units of $\hbar$) of the ion (Rb$^+$ or H$^+$) on the RbH surface, and α is the coupling constant with the dimension of energy. The Hamiltonian can also be written in terms of spherical basis

$$H = \alpha \sum_{q=0,1,-1} (-1)^q S_q K_{-q} \tag{2.68}$$

where the spherical components S_q of $\mathbf{S}$ are defined as

$$S_1 = -\frac{S_x + iS_y}{\sqrt{2}} = \frac{-S_+}{\sqrt{2}} \tag{2.69}$$

$$S_0 = S_z \tag{2.70}$$

$$S_{-1} = \frac{S_x - iS_y}{\sqrt{2}} = \frac{S_-}{\sqrt{2}} \tag{2.71}$$

where $S_x + iS_y = S_+$ is the raising operator and S_x - $iS_y = S_-$ is the lowering operator. The spherical components of K_q are similarly defined. Eq.(2.68) can also be written in terms of raising and lowering operators

$$H = \alpha \left(S_z K_z + \frac{1}{2} S_+ K_- + \frac{1}{2} S_- K_+ \right). \tag{2.72}$$

The terms $S_+ K_-$ and $S_- K_+$ in Eq.(2.72) are responsible for the angular momentum exchange between the nuclear spins on the RbH surface and the s-electron spins of the adsorbed ^{87}Rb atoms, and the term $S_z K_z$ in Eq.(2.72) is responsible for the EPR frequency shift of the gas phase ^{87}Rb atoms observed in the present experiment (see section 2.4.4). The fact that the exchange enhanced coupling constant of the Fermi contact interaction of the s-electron of the adsorbed alkali atom with the nucleus of the alkali ion is much larger than that with the nucleus (proton) of the hydrogen

ion on the RbH surface [46], implies that the angular momentum flows more easily from the polarized alkali vapor to the alkali nuclei than to the protons on the alkali hydride surface, resulting in a larger alkali nuclear polarization on the alkali hydride. The experimental evidence for this is the observation that in a cell filled with spin polarized Cs vapor and coated with CsH salt, the Cs nuclei on the CsH surface were found to be polarized, and that the NMR signal of the Cs nucleus is much larger than that of the proton [29, 47]. Therefore, it is reasonable to assume that the Rb nuclear polarization on the RbH surface in our experiment is much larger than the proton polarization. Because of this and, again, because of the much larger coupling constant of the s-electron of the adsorbed ^{87}Rb atom with the Rb nucleus than that with the proton on the RbH surface, frequency shifts observed in our experiment are probably contributed mainly by the Rb^{+} nuclei on the walls. However, we would like to point out that this assumption is not important in our analysis.

2.4.3   Coupling Constant

The coupling constant of the Fermi contact interaction between the s-electron of a Rb atom and the Rb ion on the RbH surface has not been measured nor calculated. I will make a rough estimate in the following by comparing it with the coupling constant between the s-electron of a Rb atom and the Kr nucleus, which has been measured and calculated [46]. The coupling constant of the Fermi contact interaction between the s-electron of an alkali atom and the nucleus of a noble gas atom B is given by [45]

$$\alpha = (16\pi/3)g_n\mu_n\mu_B u_1(B)^2\eta^2 \ , \tag{2.73}$$

where μ_B and μ_n are the Bohr magneton and the nuclear magneton, respectively, and g_n is the nuclear gyromagnetic ratio, $u_1(B)$ is the s-electron wave function evaluated at the atom B and η is the exchange enhancement factor, which is given by

$$\eta(R) = 1 - \sum_{i=2}^{n} \frac{\langle u_i \mid u_1 \rangle u_i(B)}{u_1(B)} \tag{2.74}$$

where R is the internuclear separation, $\langle u_i | u_1 \rangle$ is the overlap integral between the spin-orbitals u_i of the atom B and the spin-orbital of the 5s electron of the Rb atom. The spin-orbital is the product of the wave function in the spin space and the wave function u_i in the coordinate space, and $u_i(\mathrm{B})$ is the amplitude of the i-th orbital at atom B. Since only the s-orbitals have non-zero amplitude at the nucleus B, the summation in Eq.(2.74) only includes the s-orbitals of atom B. Furthermore, the overlap integral is non-zero only if the spin parts of the spin-orbitals are the same. A good approximation to atomic wave functions is to use the hydrogenic wave function with the nuclear charge Z being replaced by $Z-s$, where s is the screening constant to account for the screening of the other electrons. The energies calculated from these wave functions are in good agreement with measured values when an appropriate choice of the screening factors s is used. Listed in Table I are the values of each term in the summation in Eq.(2.73), i.e. the contribution from each s-orbital, calculated

by Herman [45] using these hydrogen-like wave functions. Note that each s-orbital has a suitable nuclear charge parameter $Z - s$.

Table I. Contributions from each s-orbital to the enhancement factor η (see Eq.(2.74)) within the approximation of hydrogenic wave functions, each orbital with an effective nuclear charge parameter.

Orbitals	$1s$	$2s$	$3s$	$4s$
Summand	8	-16	24	-32

From Table 1. we have

$$\eta_{He} = 1 - 8 = -7 \qquad (2.75)$$

$$\eta_{Ne} = 1 - 8 + 16 = 9 \qquad (2.76)$$

$$\eta_{Ar} = 1 - 8 + 16 - 24 = -15 \qquad (2.77)$$

$$\eta_{Kr} = 1 - 8 + 16 - 24 + 32 = 17 \qquad (2.78)$$

Therefore, within the approximation of hydrogenic wave functions for the s-orbitals, each with an effective nuclear charge parameter Z-s, the contribution from each s-orbital to η does not depend on the nuclear charge parameter, which cancels out. Thus, in this approximation η is exactly the same for the isoelectronic pairs Rb-Kr and Rb-Rb$^+$. The estimates of η in the above approximation, however, are too

small when compared with the measured values, becoming worse as Z increases. For example, for the Rb-Kr pair, the measured value of η is 44 [48]. This is because for noble gas atoms with large Z, the actual s-orbitals are more peaked at the nucleus than the hydrogenic wave functions used in the above. All the differences between the Rb-Rb$^+$ pair and the Rb-Kr pair are due to the fact that the Rb$^+$ nucleus is more positively charged than the Kr nucleus by one unit. This one extra unit of charge will slightly affect the energies of each orbital as well as the orbitals themselves. We can get an idea as to how big the change caused by this extra unit of charge is by comparing the energies of the s-orbitals of Rb$^+$ and Kr. Table II shows the energies of the occupied s-orbitals in free Kr and Rb$^+$ in Rb metal [49]. Note that the core orbital energies of Rb$^+$ relative to the vacuum level are obtained by adding the Rb work function of 2.16 eV to the listed core orbital energies. Since only s-orbitals have nonzero amplitudes at the nucleus, they are the only ones that contribute to the enhancement factor η and therefore only the energies of these orbitals are listed in the table. As can be seen from the table, the error in replacing the s-orbital energies of Rb$^+$ by the corresponding ones of Kr decreases from 16% for the 4s-orbital to only 6% for the 1s-orbital.

Table II. The energies of the occupied s-orbitals in free Kr and Rb$^+$ in Rb metal. The energies are given relative to the vacuum level for Kr and relative to the Fermi level for Rb [3].

Element	$1s$	$2s$	$3s$	$4s$
^{36}Kr	14326	1921	292.8	27.5
^{37}Rb	15200	2065	326.7	30.5

We would like to address whether the occupied orbitals of the Rb^+ ions in the RbH salt can be approximated by the occupied orbitals of the Rb^+ ions in the Rb metal, the energies of which are listed in the above table. It is true that different chemical environment will cause a shift, the so-called chemical shift, in the core level energy. However, this chemical shift is typically only a few percent or less, even for ions on the surface, which see a slightly different environment from ions in the bulk [50–55]. From the definition of η (Eq.(2.74)), which is quadratic in the wave functions of the noble gas orbitals, one sees that the percentage of change in η due to the change in the wave function should be comparable to the percentage of change in the energy. The percentage of change in energy is the expectation value of the Hamiltonian and therefore also quadratic in the wave function. In summary, it seems reasonable to assume that the η for the isoelectronic pairs Rb-Kr and Rb-Rb^+ probably will not differ by more than 30%.

2.4.4 Phase Shift Due to Wall Collisions

A simple semi-classical way to understand this frequency shift is the following. The coupling constant α depends on the distance between the adsorbed ^{87}Rb atom and the Rb$^+$ nucleus on the surface and therefore varies while the ^{87}Rb atom bounces around on the RbH surface. As a first approximation we will assume α to be constant, equal to its average value. The Hamiltonian $\alpha\mathbf{S} \cdot \mathbf{K}$ can be written as $-\mu_S \cdot \alpha\mathbf{K}/g_S\mu_B$, where $\mu_S = -g_S\mu_B\mathbf{S}$ is the magnetic moment of the s-electron, μ_B being the Bohr magneton and g_s the electron g-factor. Thus the Fermi contact interaction can be regarded as a precession around a magnetic field $\alpha\langle K_z\rangle/g_S\mu_B$. The average phase shift due to the precession around this field during the average dwell time τ_s for the adsorbed Rb atom in the $I + 1/2$ level is

$$\delta\phi_s = \frac{2\pi(\alpha/h)\langle K_z\rangle\tau_s}{2I + 1} \tag{2.79}$$

where the slowing-down factor $1/(2I + 1)$ is due to the fact that we assume the total angular momentum $\mathbf{F} = \mathbf{S} + \mathbf{I}$ of the Rb atom during the interaction is conserved, where $\mathbf{I}(I = 3/2)$ is the nuclear spin of the adsorbed ^{87}Rb atom.

The phase shift experienced by a Rb atom during its collision with polarized walls can also be understood quantum mechanically as follows. We assume the RbH surface is fully polarized. Consider a system consisting of the s-electron of the incoming Rb atom and the Rb nucleus on the RbH surface. Suppose the state of the system is

$\alpha_1 \alpha_2$ before collision, where α_1 represents the spin-up state of the s-electron and α_2 the spin-up state of the Rb nucleus. At the end of the wall collision the wave function of the system is given by

$$e^{-\frac{i}{\hbar}\alpha \mathbf{S}\cdot\mathbf{K}\tau_s}\alpha_1\alpha_2 = e^{-\frac{i}{2\hbar}\alpha(\mathbf{F^2}-\mathbf{S^2}-\mathbf{K^2})\tau_s}\alpha_1\alpha_2 = e^{-i3\bar{\alpha}\tau_s/4\hbar}\alpha_1\alpha_2 \qquad (2.80)$$

where we have assumed total spin F is a good quantum number since we are considering wall collisions in which the s-electron spin does not flip. Thus the phase shift

$$\delta\phi_s = 3\alpha\tau_s/4\hbar \qquad (2.81)$$

The coherently accumulated phases during repeated wall collisions give rise to a EPR frequency shift of the Rb atom. The method for measuring the average phase shift of spin polarized Rb atoms during each wall collision consists of measuring the EPR frequencies $\omega^{(+)}$ and $\omega^{(-)}$ corresponding to σ^+ and σ^- pumping beams of the same intensity for a number of different cell lengths L. We show that the difference between these Larmor frequencies $\Delta = \omega^{(+)} - \omega^{(-)}$ depends linearly on $1/L$, and the slope yields the ensemble-averaged phase shift experienced by a spin polarized Rb atom while adsorbed on the RbH surface.

Chapter 3

Experiment

3.1 Experimental Method

3.1.1 Evanescent Wave

One of the unique features of our experiment is the use of evanescent wave to probe the polarization of the Rb vapor. Since the penetration depth of the evanescent beam is $\sim 10^{-4}$ cm, the evanescent wave probing is independent of the cell length, which varied between 70 μm and 0.24 cm depending on the experimental setup. By using linearly polarized evanescent probe beam we measured the Faraday rotation signal, which is proportional to the vapor polarization. It is important that s-polarized instead of p-polarized evanescent beam be used. This is because of the following property of the evanescent wave [56]. If the incident beam is s-polarized, then the evanescent wave is also s-polarized. On the other hand, if the incident beam is p-polarized, then the

evanescent wave is right-handed elliptically polarized in the incident plane.

3.1.2 Detection Method

As a linearly polarized light passes through the polarized Rb vapor, its polarization plane is rotated by a certain angle, $\Delta\theta$, from its original polarization plane, due to the polarization of the Rb vapor. This phenomenon is called paramagnetic Faraday rotation. In our case the incoming light is our probe beam and is s-polarized. The incoming light can be decomposed into left (σ^+) and right (σ^-) circularly polarized light. These opposite polarizations see different indices of refraction, $n_+^{'}$ and $n_-^{'}$. The difference in these indices of refraction causes the left and right circularly polarized components to propagate at different speeds, resulting in a rotation of the original polarization plane. The Faraday rotation angle is given by

$$\Delta\theta = \pi\frac{(n_+^{'} - n_-^{'})l}{\lambda} \tag{3.1}$$

where l is the path length and λ is the wavelength. In this experiment the change in the Faraday rotation angle is monitored. The amplitude of the rf is modulated with a square wave at a frequency $\Omega/2\pi = 200$ Hz. The frequency of the rf is stepped across the Rb EPR curves, using a frequency generator from Stanford Research Inc., and the signal is measured at each of these frequencies. Typically the function generator output stayed at each frequency for about 4 sec. The signal was averaged in that

time interval and was fitted with a Lorentzian.

Our method of detection used a combination of a half-wave plate and a Wollaston prism. The rotated probe light (due to Faraday rotation), after exiting the cell containing the polarized vapor, passes through a half-wave plate. The half-wave plate is used such that the angle of polarization can be rotated before passing through the Wollaston prism. The half-wave plate decomposes the light into two components and changes the relative phase of of the two components by π, thus changing the angle of polarization.

The Wollaston prism splits the incoming beam into two orthogonal components the following way. It is composed of two right angle prisms. The prisms are made of uniaxial birefringent crystal. The two prisms are stacked together using cement in such a way that their optical axes are orthogonal to each other. Furthermore, their optical axes are parallel to the entrance and exit surfaces for the beam as shown in Fig. 3.1. If the incoming linearly polarized beam has a component parallel to the optical axis (the e-ray with an index of refraction of n_e) and a component orthogonal to the optical axis (the o-ray with an index of refraction n_o), after passing through the first right angle prism, the e-ray becomes o-ray and the o-ray becomes e-ray so that one bends toward the normal whereas the other bends away from the normal. The result is that the two components will emerge separated, with orthogonal polarizations.

The half-wave plate was used in the cancellation stage. Before we polarized the Rb vapor, we needed to adjust the half-wave plate so that the two components coming

from the Wollaston prism had exactly the same intensity. The physical reason for this cancellation is that due to the slight birefringence of the optical components such as windows, prisms, etc, the incident s-polarized beam could be slightly rotated after passing through the cell even when the Rb vapor was not polarized. Thus, the cancellation procedure was used to cancel this small rotation.
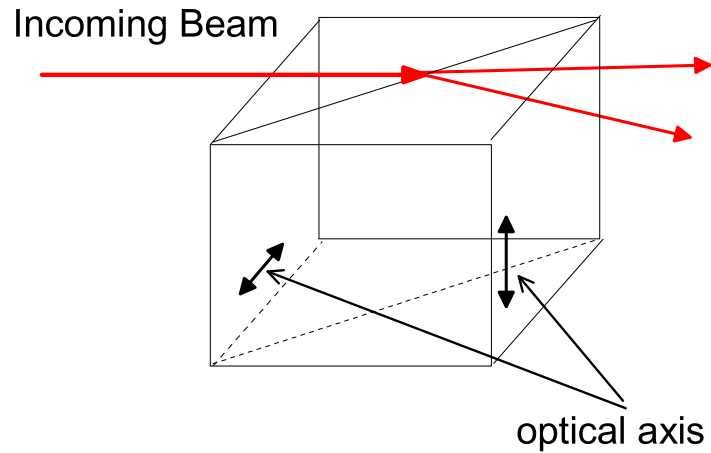

Incoming Beam

optical axis

FIG. 3.1. An incoming beam (red line) is decomposed into two orthogonal components at the interface of two uniaxial crystals with perpendicular optical axes in the Wollaston prism as described in the text.

The two component beams, after the Wollaston prism, were detected by two identical photodiodes. The outputs of the photodiodes were sent to a Lock-In Amplifier

which outputs a differential signal from the photo-detectors. The differential method

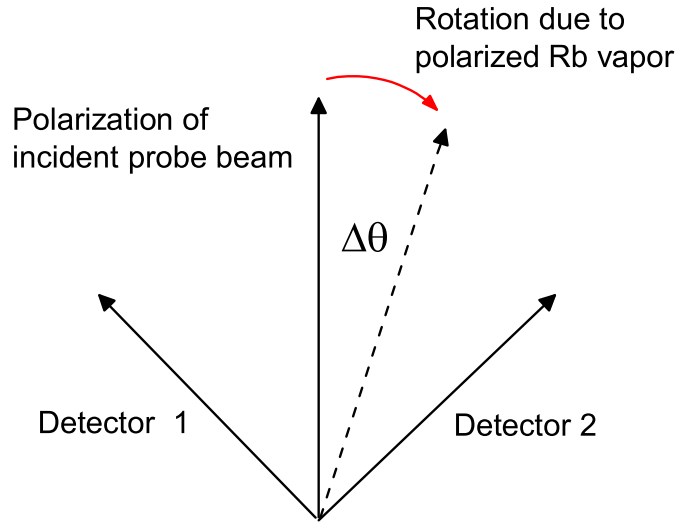of detection is an ideal method in reducing (canceling) noise from the signal.

FIG. 3.2. After passing through polarized Rb vapor the polarization plane of the incident probe beam is rotated by an angle $\Delta\theta$, the Faraday rotation angle. The signals seen by detector 1 and detector 2 are given by Eq.(3.2) and Eq.(3.3).

The following is a more detailed discussion of the detection method. Referring to

Fig. 3.2, when the Rb vapor was unpolarized, the two detectors see the same signal

and therefore their difference is zero. Suppose the polarization of the light beam,

after passing through the polarized Rb vapor, is rotated by an angle $\Delta\theta$, the Faraday

rotation angle, then detector 1 and detector 2 see the following signals:

$$S_2 \propto \cos^2\left(\frac{\pi}{4} - \Delta\theta\right) \ , \qquad\qquad (3.2)$$

$$S_1 \propto \cos^2\left(\frac{\pi}{4} + \Delta\theta\right) \ . \qquad\qquad (3.3)$$

The difference of these two signals is proportional to $\sin(2\Delta\theta)$. Since the Faraday rotation angle is normally $\ll 1$, the difference in these signals is seen to be proportional to the Faraday rotation angle $\Delta\theta$.

3.2   Cell Preparation Procedures

The coating procedure for the antirelaxation coatings and the RbH-coated cells is described in the following. In each case the glass cell used was a cylindrical Pyrex glass cell with an inner diameter of 23 mm. The cells contained isotopically enriched rubidium (98.3 at. % ^{87}Rb) in the stem and various pressures of nitrogen buffer gas. The pressure is referred to 25^oC. A movable glass prism inside the cell acts as the adjustable back wall of the cell (see inset of Fig.1). Since the distance between the front and back walls is more than one order of magnitude smaller than the cell diameter, the space between the front and back walls has the shape of a thin slab. The effective cell length (L) can be varied by tapping the stage on which the cell sits.

3.2.1 Octadecyltrichlorosilane (OTS) Coating Procedure

The coating procedure for our OTS-coated cells followed a similar procedure to that as Rosen et. al. [57] and is described in detail in the following. Four different cells were made and coated simultaneously (#136.2, #137.2, #138.2, #128.3).

The cells were first rinsed three times with distilled water. Piranha solution, consisting of sulfuric acid (H_2SO_4) and hydrogen peroxide (H_2O_2), was then used in order to thoroughly clean the inside surfaces of the cell body, prism and stem. The cells were filled with Piranha solution and heated to 80°C for 30 minutes, emptied, and repeated once more with fresh Piranha solution. The cells were then rinsed three times with distilled water, two times with methanol (CH_3OH) and finally rinsed an additional two times with distilled water. The cells were then baked in an oven at 120°C for 2 hours.

A non-dry OTS with a 5 mM concentration was used to coat the cells. The cell was coated in lab air (we did not use a nitrogen sealed box). The OTS solution was added to the cells using a clean pipette and the cells were placed in a sonicating bath for 10 minutes. The OTS was dumped out of the cells and were then rinsed twice with chloroform ($CHCl_3$). On the third rinse they were again sonicated for a few minutes. The cells were allowed to drip dry for two days.

Once dried the cells were put onto a glass manifold (via glass blowing) which is attached to our pumping system. Our pumping system consisted of two pumps, a roughing pump and a turbo pump. The glass manifold had one arm which held the

mixture of $^{87}RbCl$ + Ca. The Rb in $^{87}RbCl$ is isotopically enriched (98.3% ^{87}Rb). Once the cells were fused onto the manifold the cells were baked at 190°C for 12 hours with the pumping system on in order to pump away the desorbed impurity gases.

Before the ^{87}Rb was distilled into the cells, it was degassed by baking the $^{87}RbCl$ + Ca arm in an oven for two and half hours at 170-390°C. The degassing process helps to get rid of any gas which otherwise might have got into the cells. The reaction of the $^{87}RbCl$ + Ca mixture started when the temperature of the mixture was raised to about 526°C. The temperature of the oven, in which the $^{87}RbCl$ + Ca mixture was located, was kept at 554°C for one hour. The reaction of the $^{87}RbCl$ + Ca mixture released the ^{87}Rb metal, which was then chased using the blow torch into the stem of the cells. It was important that none of the ^{87}Rb got on the front surface of the cells and instead was confined in the stem (reservoir) of the cells. To ensure this, hot air was blown onto the front surface of the cells, driving the ^{87}Rb to the stems. The cells were filled with nitrogen (N_2) with a pressure of 5 Torr (referring to room temperature). Lastly, the cells were pulled off of the manifold and our experimental cell (#128.3) was heated in the oven for ten hours, with the stem (tip) at room temperature and the body temperature at $\sim$ 70°C. The process of curing the Rb cell is not fully understood, although the curing may help the Rb vapor come into equilibrium with the coating.

3.2.2 Paraffin Coating Procedure

The coating procedure of the paraffin coated cell (#160) follows [58, 59] and is described in the following.

The glass cell used is the same type as that used in the OTS experiment, although the cleaning procedure for this cell differs from that of the OTS coated cells. The cell was rinsed twice with distilled water and then cleaned twice with a hydrochloride (HCl) solution with a 12 M concentration (this corresponds to 10% HCl, 12.4 mL HCl and 36.6 mL H_2O). The cell was then rinsed twice with distilled water and finally nitrogen gas was used to dry the cell.

The cell was attached to the glass manifold (via glass blowing) which had an arm containing the paraffin and was attached to the pumping system. The pumping system was turned on (both the turbo and roughing pumps) and the pressure of the manifold was pumped down to 10^{-7} Torr. This pressure was sufficiently low such that it ensured there were no leaks in the glass manifold.

Using hot air the paraffin was driven from the manifold arm to the stem of the cell. The cell was then pulled off of the manifold and the paraffin was driven further down into the body of the cell, again, using hot air and was baked for a total of 10 hours with a temperature range of 200-338°C. During baking the cell was checked intermittently to ensure that the paraffin was not settling in the corners of the cell body. It was important to bake the cell at a high enough temperature such that the paraffin could vaporize and coat the cell walls. After baking, the body of the cell was

cleaned completely of any paraffin using a torch where any excess paraffin was driven to the very tip of the stem. The tip of the stem was then broken off, which enabled us to get rid of the excess paraffin.

The cell (now coated with paraffin) was attached to a second glass manifold which had an arm for the ^{87}RbCl + Ca mixture. The cell was baked on the manifold at 70°C for 3 hours and the system was then pumped for 12 hours. Using a torch, the path of the manifold in which the Rb was to travel was cleaned. This was necessary in that it was important that the Rb being distilled into the cell did not react with any paraffin on the inside wall of the manifold. Using a magnetic slug the breakable seal of the ^{87}RbCl + Ca arm was broken. The ^{87}Rb was finally distilled into the stem of the cell and pulled off of the manifold. The cell was cured at 65°C for 60 hours in an oven with a small fan, which was used to ensure that there was a very small temperature gradient inside the oven. Curing of the cell continued at 70°C in our experimental oven for an additional 10 hours.

3.2.3   RbH Coating Procedure

In order to make the RbH coated cells, the procedure used in [29] was closely followed. The cells used were of the same type used in the OTS and paraffin experiment (a one inch length Pyrex glass cell with a 1/16th inch optical window and a movable prism inside). The cells were cleaned using the same procedure as the OTS-coated cells in section 3.2.1, but without the use of Piranha solution. Two cells (#161 and

#162, where # 162 was used for our data) were attached to a glass manifold via glass blowing. The glass manifold consisted of two arms one in which the natural Rb was held and a second for the ^{87}RbCl + Ca mixture. Next, the ^{87}RbCl + Ca mixture was added to the designated manifold arm which was then attached to the pumping system. An ampoule containing the natural Rb was broken and then dropped into the manifold arm, which was then sealed.

The pumping system was turned on and the manifold was pumped down to a pressure of 7.7×10^{-8} Torr, indicating that there were no leaks in the manifold. Next, the cells were heated for 17 hours at 450°C and the arms were de-gassed using a hot air gun. Once the system was cooled down, the natural Rb was distilled into the arms. It is important to note that when the natural Rb was distilled into the cells a bluish coating was visible inside the cells. Once the natural Rb was in the body of the cells the manifold was filled with 829 Torr of H_2 and the cells were heated for 12 hours at 150°C. The process of heating allowed for the Rb and hydrogen to react and form RbH. The procedure described above differs from that of ref. [29] in that Ishikawa et. al. conducted the coating cycle four times, whereas in our case the cycle was done once. Therefore, we estimated the RbH thickness in our cells was about 2.5 μm, which was 1/4 of the thickness in ref. [29]. After the system cooled it could be seen that one cell was a bit foggier than the other, indicating that it had a thicker coating of RbH. The thicker coated cell was not usable for this experiment because the intensity of the transmitted evanescent probe beam was too weak, as there was

too much scattering due to the thicker layer of RbH on the surface of the optical window.

Before the ^{87}Rb could be distilled into the cells, it was important to ensure that there was no RbH in the pathway because RbH contained natural abundance Rb, thus the heat generated in the process of distillation of ^{87}Rb into the cells would cause the RbH (in the manifold) to dissociate, causing ^{85}Rb to get into the cells thereby reducing the percentage of ^{87}Rb in the signal. In order to get rid of any RbH in the distilling pathway of ^{87}Rb, the RbH was annealed. To do this, the system was filled with hydrogen and heated (not including the ^{87}RbCl + Ca arm) to about 180°C for 2 1/2 hours (the annealing pressure of the hydrogen was 840 Torr). After the system was cooled the H$_2$, was pumped out and the ^{87}RbCl + Ca arm was heated to 540°C for one hour (this was the temperature at which the ^{87}Rb distilled out of the arm) and a torch was used to distill the rubidium into the stems of the cells. The cells were then filled with 5 Torr N$_2$ and pulled off the manifold. Once the cells were removed from the manifold the bodies of the cells were further heated in order to drive some of the ^{87}Rb that may have gotten into the body back into the stem of the cell. This was done at 62°C for approximately 24 hours.

3.3 Experimental Setup

The experimental set-up is similar in the dwell time experiment and the surface phase shift experiment. I will describe the experimental set-up for the dwell time experiment, which will be followed by a short description of the surface phase shift experiment in which I point out the differences in the set-up.

3.3.1 Experimental Setup for the Study of Antirelaxation Coating

The experiments are set-up and performed on an optical bench. The experimental cell sat inside of a PEEK oven which was inside a Teflon oven as can be seen in Fig.3.4. The cell was heated by flowing hot air into the oven in order to avoid ohmic heating, which would generate unwanted magnetic fields. The cell was positioned towards the back of the PEEK oven and a prism was placed in front of the cell (externally). The external prism was pressed against the front surface of the cell which allowed the pump and probe beams to be evanescent waves. A layer of index-matching oil, with an index of refraction n = 1.45, was dropped between the front surface of the cell and the back surface of the outside prism, so that there was no air gap between the two surfaces, which is important for the use of evanescent waves. In order for both the pump and probe beams to undergo total internal reflections the beams needed to enter the cell close to each of their respective critical angles. The ovens were positioned on

a a micrometer-driven rotation stage with a resolution of 33 millidegrees in order to adjust the incident angle at which the beams entered the prism. We were interested in the critical angle of the beam incident on the front surface of the cell, so through the following calculation we were able to relate the incident beam on the prism, α, with the incident beam on the front surface of the cell, θ, as shown in Fig. 3.3. Moreover, the determination of θ is needed in order to calculate the penetration depth, d, of the probe and pump beams.
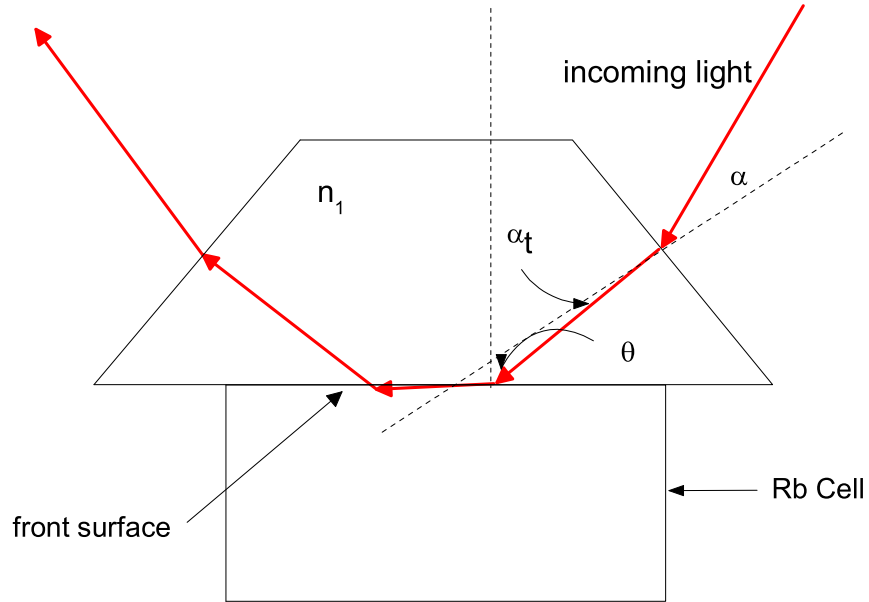

FIG. 3.3. Incoming light beam (in red) incident on the external prism of the cell. α is the angle of incidence on the prism, α_t is the angle of the light beam upon entering the prism with the normal of the prism.

At the critical angle of the interior of the prism, $\theta = \theta_c$ and $n_1 sin\theta_c = 1$. Using the exterior angle rule which says $45 = \theta + \alpha_t \rightarrow \alpha_t = 45 - 0$ along with Snell's law ($sin\alpha = n_1 sin\alpha_t$) we find at $\theta = \theta_c$ that

$$n_1 = \frac{1}{\sin\theta_c} \tag{3.4}$$

We can now write the critical angle in terms of α which we can determine from the micrometer reading,

$$\theta_c = \tan^{-1} \frac{1}{1 + \sin\alpha/\sin 45} \tag{3.5}$$

We have determined our $\alpha = 2.17^o$ and therefore we find $\theta_c = 43.50°$ and $n_1 = \frac{1}{sin\theta_c} = 1.45$. Finally, by using the relationship $sin\alpha = n_1 sin(45 - \theta)$ we can write θ in terms of α, where

$$\theta = 45 - \arcsin\frac{\sin\alpha}{n_1} \tag{3.6}$$

and therefore we can calculate θ. From θ we can determine the penetration depth of the probe and pump beams from the following relationship

$$d = \frac{\lambda}{2\pi n\sqrt{\sin^2\theta - \sin^2\theta_c}} \tag{3.7}$$

A small Teflon cap is placed on top of our PEEK oven and covers the top of the cell. The cap is necessary in that blowing hot air directly on the cell may cause damage to the coatings. We use two E-type thermocouples to monitor the temperature of

the body of the cell and the temperature of the tip of the cell (in which the ^{87}Rb is contained). It is important that the tip temperature remains several degrees cooler than the body temperature so that the Rb atoms do not condense on the surface of the body of the cell. Condensation of Rb atoms on the walls can ruin the coatings. In our experiment the cell tip was 6°C lower than the cell body temperature which was kept at 72° C and stabilized within 0.5° C. This temperature was sufficiently far away from the melting point of paraffin which is 93°C.

Three pairs of Helmholtz coils were placed around the cell. One pair served as our holding magnetic field in the z-direction while the others were used to cancel any residual fields. Another set of Helmholtz coils were wrapped around the oven to generate an oscillating (rf) magnetic field (in the y-direction). A function generator from Stanford Research Inc. was used to output a sine which was modulated by a square wave into the rf coils.

It is important to note that the rf coils have a frequency dependent impedance. As we scanned the rf from low to high the signal was asymmetric due to the impedance change. A simple way to correct this is by adding a 100 Ω resistor to the rf coil, which makes the impedance of the rf coil dominantly resistive and frequency independent. The ovens, Helmholtz coils, and rf coils were were all placed inside two layers of μ-metal shields. The diameter of the outer shield was 28 cm, and that of the inner was 25 cm. The length of the shields was 28 cm. Both ends of the shields were covered with μ-metal caps. One shield reduces the outside field by a factor of 350 and both
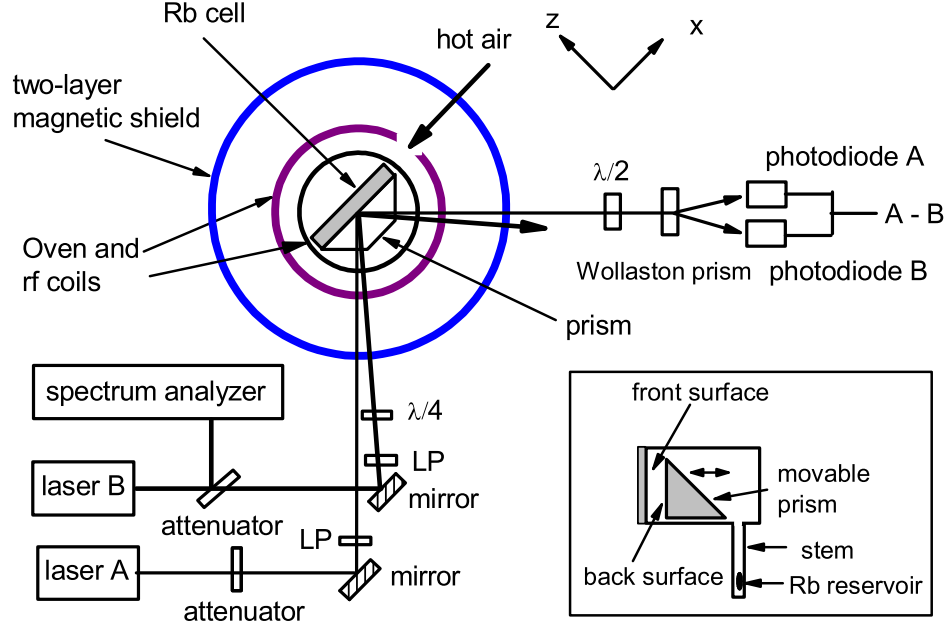
shields reduce the outside field by a factor of 25,000.

FIG. 3.4. Exerimental setup. The pump laser is circularly polarized using a Glan-Thompson linear polarizer (LP) and a quarter-wave plate ($\lambda/4$). The probe laser is s-polarized using a Glan-Thompson linear polarizer (LP). Three orthogonal pairs of Helmholtz coils (not shown) are inside the two-layer magnetic shield. Also not shown are the HeNe laser and the lens assembly used to measure the cell length by retroreflection. The holding field is alng the positive x direction. Inset: a Rb cell of adjustable length.

A single mode diode laser served as the pumping laser. The diode laser had a linewidth of 45 MHz. The ^{87}Rb atoms in the vapor were optically pumped using a σ^+ or σ^- polarized beam from a diode laser. The pump beam propagated along the $+z$ axis, and illuminated the entire cell. Its intensity was ~ 9 mW/cm^2 and its

frequency was tuned slightly ($\sim$ 600 MHz) to the high frequency side of the transitions $F = 1 \rightarrow F' = 1, 2$ of the ^{87}Rb D1 line (794.8 nm) in order to pump the vapor more uniformly. A small fraction of the pump beam was deflected using a beam splitter to pass through a separate reference cell. The reference cell was used to more easily find the correct resonance frequency (by tuning the current of the current supply) of the pump laser. This was done by watching the ^{87}Rb reference cell through an infra-red viewer indicating that the laser is tuned to resonance. The pump beam was tuned slightly off resonance in order to maximize our signal. This is due to the fact that on resonance, the pump beam would be completely absorbed by the Rb vapor atoms upon entering the cell and thus by detuning the resonance frequency of the pump, the light can polarize the entire cell. The pump beam passed through a set-up of two cylindrical lenses, the first with a focal length of 5 cm and the second with a focal length of 15 cm, which expanded the beam in the horizontal direction in order to make the pump beam as round and collimated as possible. Also, these lenses could be adjusted to help avoid any converging or diverging of the pump beam in the experimental path of the laser. The pump beam passed through a Newport $\frac{\lambda}{4}$-plate in which the laser beam (upon rotating the $\frac{\lambda}{4}$-plate 360° and monitoring the output intensity) output intensity only varies by 6.7%. We found that out of approximately 15 mW of pump beam, the intensity varied less than 1 mW. The $\frac{\lambda}{4}$-plate allowed for the circularly polarized pump beam to be alternated between σ^+ and σ^- circularly polarized light. The beam then passed through a pinhole with a diameter of 4.5 mm

and entered the cell as an evanescent beam with a penetration depth of 1.158 μm.

Not shown in the experimental set up was a spectrum analyzer, in which part of the pump beam is reflected into in order to monitor the pump beam frequency to ensure it does not drift throughout the experimental run. The output of the spectrum analyzer is sent into an oscilloscope where the peak frequency of the pump beam was monitored such that it did not drift more than 30 MHz. The current of the pump beam power supply could be fine tuned in order to pull the pump beam to the correct frequency, if in fact the pump beam frequency did drift.

A second single mode diode laser serves as the probe beam. The ^{87}Rb atoms in the vapor were probed in the vicinity ($\sim 10^{-4}$ cm) of the front surface of the cell using a weak s-polarized evanescent beam from a second diode laser tuned to the transitions $F = 2 \rightarrow F' = 1, 2$ of the ^{87}Rb D1 line. The probe beam size was about 2.0 mm in diameter. Next, the probe beam was reflected from a mirror into a linear polarizer which vertically polarizes the light. The light then passes through a prism and undergoes total internal reflection which directs the beam towards the cell. It is important that the beam going into the glass prism is not polarized 45° for the following reason: 45° light consists of s- and p-components, which upon hitting the prism see two different speeds (they have different indices of refraction) and therefore the polarization of each component will be different after passing through the prism resulting in a polarization that is not linear. The prism outside the oven (as shown in the set-up figure) is useful in that the angle between the pump and probe beam can

be very small (0.322°), allowing for a larger penetration depth of the pump beam. The probe beam enters the front surface of the cell as an evanescent beam with a penetration depth of 0.815 μm.

It is necessary that the pump and probe beam are overlapping in the cell (i.e. that they are hitting the same spot on the front surface of the cell) to ensure that all of the atoms being probed are being pumped (polarized), resulting in a maximum signal. Prior to putting the cell in the experimental oven, a small rod was installed in the location of the front surface of the cell. The pump and probe beams were aligned such that they overlapped on the rods location.

A HeNe laser is used to measure the cell thickness by retroreflection with an accuracy of 20μm. The method of retroreflection is the same method which was used by Thomas, et. al. [60]

The procedure for obtaining the EPR curve was as follows. The frequency was stepped using a computer program which sent an output signal to the function generator telling the function generator to step. The stepping program allowed us to tell the function generator how large of a frequency step to take, how long to stay on each frequency and how many steps to take. For the OTS coated cell we took frequency steps of 160 Hz (a scanning range of 8 kHz), 120 Hz (a scanning range of 6 kHz), 40 Hz (a scanning range of 1 kHz) or 32 Hz (a scanning range of 800 Hz) depending on the cell length (for thinner cells the linewidths are much broader and therefore we needed to scan a larger range in order to see a full resonance curve). For

each resonance curve, 50 points (or steps) were taken in which each scan took 200 seconds, thus, we stayed on each frequency for 4 seconds. It is important to note that the Lock-In amplifier has a time constant τ which was set to 30 ms, meaning that the Lock-In amplifier is doing its own averaging for 30 ms, and so 4 seconds is sufficiently larger than the averaging time, τ of the Lock-In amplifier. A resonance curve was produced on the oscilloscope (for all the cell lengths, and for both $\sigma+$ and $\sigma-$ pumping light) and was then downloaded onto our computer. The resonance curves were analyzed by averaging the middle points of each frequency step and throwing away points close to the instant the frequency changes, because at those instances the function generator creates a spike due to the sudden change of frequency.

3.3.2   Experimental Setup for the Study of RbH Coating

The experimental setup Fig.3.5 for the RbH experiments was similar to that of the OTS and paraffin set-up except for the following difference. In cells coated with alkali hydride, the wall relaxation rate for polarized Rb atoms is much faster than in cells coated with antirelaxation coatings. In fact the reason that the alkali hydride coating can be polarized is because of the angular momentum transfer from the polarized Rb atoms in the vapor to the alkali hydride surface. Thus the signal to noise ratio is much worse than in cells coated with antirelaxation coatings. Therefore the pumping laser used in the RbH experiment was not an evanescent wave, but illuminated the entire cell in order to achieve larger Rb vapor polarization, which in turn produces
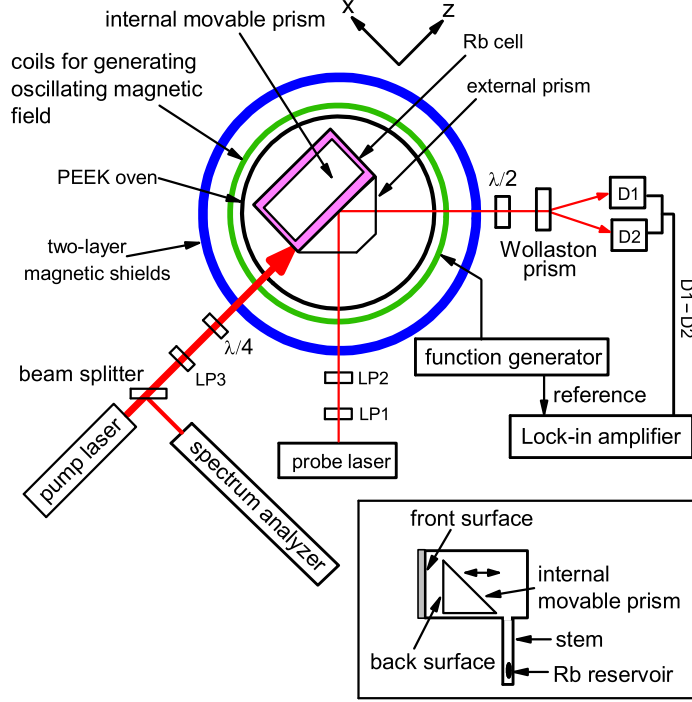
larger wall polarization and larger frequency shifts.

FIG. 3.5. Experimental setup (top view). The pair of Glan-Thompson linear polarizers LP1 and LP2 is used as an adjustable attenuator and also ensures that the probe beam is s-polarized. The linear polarizer LP3 and the $\lambda/4$ waveplate are used to produce a σ^+ or σ^- pump beam. Not shown in the figure are the HeNe laser and lens assembly used to measure the cell length by retroreflection. Inset: a Rb cell of adjustable length (side view).

As in section 3.3.1 the cell was also heated by blowing hot air into the oven except the temperature was significantly higher.

Chapter 4

Experimental Results

4.1 Experimental Results for Antirelaxation-Coated Walls

The experimental data for OTS-coated walls were taken in cell #128.3 and those for paraffin-coated walls were taken in cell #160. The data were analyzed using Eq.(2.11):

$$\frac{2L}{\bar{v}} = -2\delta\phi_s\frac{1}{\Delta} - \tau_s. \tag{4.1}$$

Plotted in Fig. 4.1 is the dependence of $2L/\bar{v}$ on $1/\Delta$. As one can see the data can be fitted quite well with a straight line. The y-intercept is equal to the negative of the dwell time, which is found to be $\tau_s = 0.9 \pm 0.1$ μs. The slope represents the sum of the surface phase shift and the phase shift due to the evanescent pump beam.

Since the phase shift due to the surface is negligibly small for antirelaxation coatings, the slope in Fig. 4.1 is equal to the light shift of the evanescent pump beam. This was shown in [61]. Our data were taken over a one hour period. For each cell length L, we measured the peak frequencies of the EPR curve for $\sigma+$ and $\sigma-$ circularly polarized light, from which we obtained Δ. Data in paraffin-coated walls were obtained in a similar fashion and were plotted in Fig. 4.2. The much larger slope in Fig. 4.2 is due to the large intensity of the pump beam and the y-intercept yields a dwell time of τ_s = 1.84 $\pm$ 0.34 μs for paraffin-coated walls.
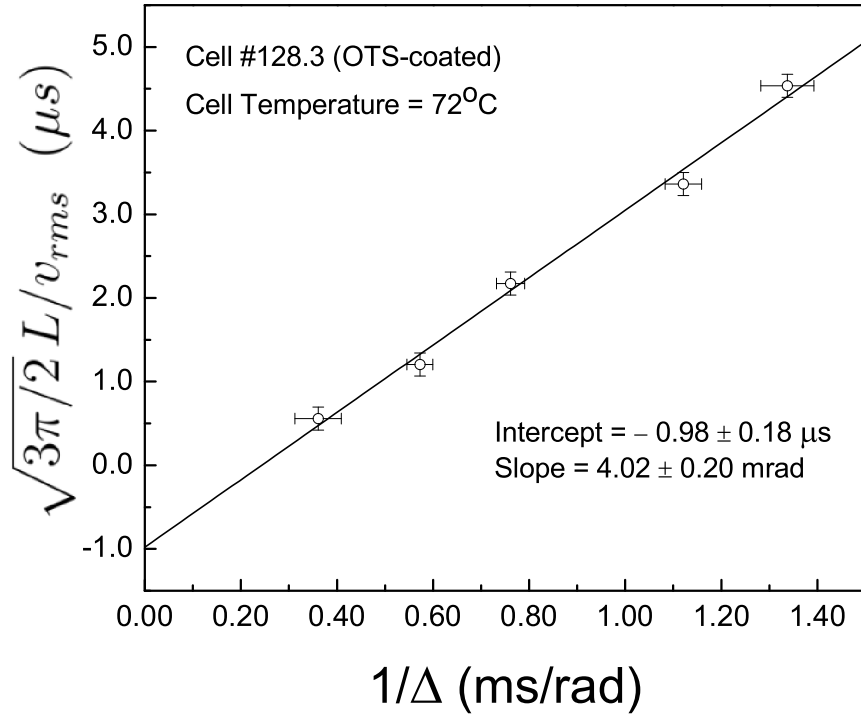

FIG. 4.1. A representative plot of cell length L versus $1/\Delta$ for a cell coated with OTS and filled with 5 Torr N_2 buffer gas.

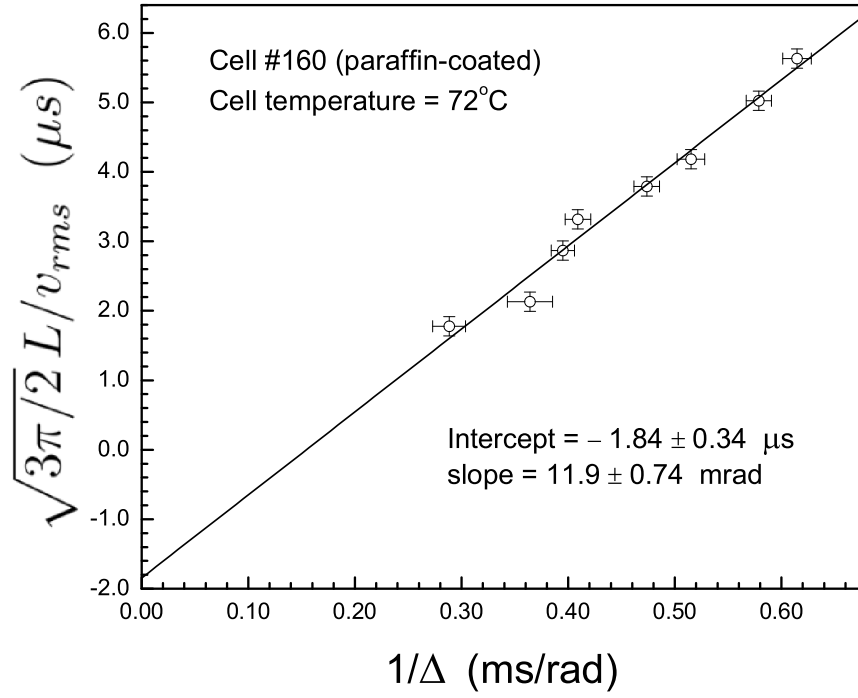It is interesting to compare the dwell times for OTS and paraffin coatings. The

FIG. 4.2. A representative plot of cell length L versus $1/\Delta$ for a cell coated with paraffin and filled with 5 Torr N_2 buffer gas.

dwell time for OTS is shorter than that for paraffin, whereas the relaxation probability

for OTS is larger than that for paraffin by almost one order of magnitude. This

implies that the superior antirelaxation property of paraffin is not because of an

extremely short dwell time of spin polarized Rb atoms in paraffin, but because the

average strength of the interactions experienced by them while they are inside paraffin

is much weaker than while they are inside OTS. The OTS coating is only several

nanometers thick [19], unlike paraffin coating, which is coated with vapor and tends

to be thick. Thus, for wall collisions of longer dwell time, spin polarized Rb atoms may

diffuse to the sites near the interface between the glass surface and OTS and become

depolarized. These Rb atoms, upon leaving the OTS coating, will not contribute

to the signal. Thus the long dwell time tail of the dwell time distribution of Rb

atoms is truncated, resulting in a shorter average dwell time. It was reported that the OTS coating does not completely cover the bar glass surface [62]. The Rb atoms can occasionally collide with these bare glass patches and become depolarized. The relaxation of Rb atoms near the interface and on bare glass patches can help explain the larger relaxation probability of Rb atoms on OTS coatings.

In their study, Bouchiat and Brossel also measured the correlation time of the dipole-dipole interaction, which they found to be $\tau_{c1} \sim 4 \times 10^{-10}$ sec [18]. In our study of OTS- and paraffin-coated walls we measured a much longer dwell time on the order of $\sim 1\mu s$. The longer dwell time measured in my study may be due to trapping of the Rb atoms inside the coating [61], as it is well known that alkali atoms are known to diffuse into coatings [64, 65]. One encounters a similar situation in the case of ^{129}Xe in cells coated with Surfasil, also an antirelaxation coating. It was found that the ^{129}Xe atoms can be trapped inside the coating for as long as 10 μs [63].

From the dwell time τ_s we can estimate the total number of alkali atoms N_c trapped in the coating per square centimeter in equilibrium to be $N_c = nl\tau_s/\tau_b$, where n is the alkali vapor number density and l the characteristic dimension of the cell. Using $\tau_b \sim l/\overline{v}$, where $\overline{v} = \sqrt{8kT/\pi m}$ is the mean speed of Rb atoms, the estimated number of alkali atoms trapped in the coating per square centimeter is $N_c \sim n\tau_s\overline{v}$. For example, for paraffin-coated cells with cell temperature of 72°C, we have $\tau_s \sim 2$ μs, $n = 8.0 \times 10^{11} cm^{-3}$, and $\overline{v} = 2.9 \times 10^4 cm/s$. Thus $N_c \sim 5 \times 10^{10}$ cm^{-2}.

4.2   Experimental Results for RbH-Coated Walls

4.2.1   Measured EPR Frequency Shift

The EPR frequencies measured in the present experiment for σ^+ and σ^- pumping can be written as

$$\omega^{(\pm)} = \omega_0 \pm \delta\omega_{\text{light}} \pm \delta\omega_s, \tag{4.2}$$

where ω_o is the EPR frequency of the ^{87}Rb atom due to the holding field, $\pm\delta\omega_{light}$ is the light shift due to $\sigma^\pm$ pump beam, and $\pm\delta\omega_s$ is the frequency shift due to wall collisions for $\sigma^\pm$ pumping. As mentioned before, since we pump the ^{87}Rb atoms from the $F = 1$ level and probe the Zeeman resonances of the $F = 2$ level, we have $\delta\omega_{light} < 0$ [66]. That is, the Stark effect causes a negative frequency shift for σ^+ pumping and a positive one for σ^- pumping. The opposite is true for the frequency shift due to collisions with polarized walls.

Shown in Fig.4.3 is the dependence of the measured EPR frequency shifts $\omega^{(\pm)} - \omega_o$ on the cell length L. The values of ω_o as obtained from $\omega_o = (\omega^{(+)} + \omega^{(-)})/2$ for each L fluctuate around its mean, which is used in Fig.4.3, by no more than $2\pi \times 24$ rad s^{-1}. We note that $\omega^{(\pm)} - \omega_o$ is expected to approach a constant $\pm\delta\omega_{light} = \mp 2\pi \times 240$ rad s^{-1} for large L, when the frequency shift due to wall collisions becomes negligible. One sees that for small L the freuqency shift due to wall collisions outweighs the light shift and $\omega^{(+)} > \omega^{(-)}$ whereas for large L the apposite is true and we have $\omega^{(-)} > \omega^{(+)}$, in agreement with the semiclassical theory of light shift [66]. The observation that the

difference $\omega^{(-)} - \omega^{(+)}$ in the measured EPR frequencies changes sign from negative to positive as the cell length L increases proves that the observed frequency shift is not owing to gas phase processes but to collisions with cell walls.

Further evidence is provided by the data shown in Fig.4.4, which displays a pair of ^{87}Rb magnetic resonance curves taken under the same experimental conditions but in an OTS-coated cell. One sees the dramatic difference between the data taken in RbH- and OTS-coated cells. In RbH-coated cells, we have $\omega^{(+)} > \omega^{(-)}$ for cell length ≤ 0.18 cm whereas in the OTS-coated cell, which has a cell length of 0.094 cm, we still have $\omega^{(+)} < \omega^{(-)}$, indicating that the light shift still dominates. In fact, in OTS-coated cells, under any of our experimental conditions, we have not observed $\omega^{(+)} > \omega^{(-)}$, implying that the EPR frequency shift due to collisions with OTS-coated walls is not detectable in the present experiment. The striking difference between the data taken in RbH- and OTS-coated cells and the cell length dependence of the frequency shift conclusively rule out any gas phase process as the cause of the observed frequency shift, and unambiguously prove that the observed frequency shift is due to collisions with RbH-coated walls.

The light shift $\delta\omega_{light}$ from Eq.(4.2) is obtained by measuring $\omega^{(-)}$ and $\omega^{(+)}$ in an OTS-coated cell (Fig. 4.4), in which the shift due to wall collisions is negligible. Thus we have $\delta\omega_{light} = \Delta/2 = $ -$2\pi \times$ 240 rad s^{-1}.

The frequency shift due to wall collisions in RbH-coated cells can be computed from Eq.(2.21) for each value of L. For example, for $L = 0.138$ cm, we found from the
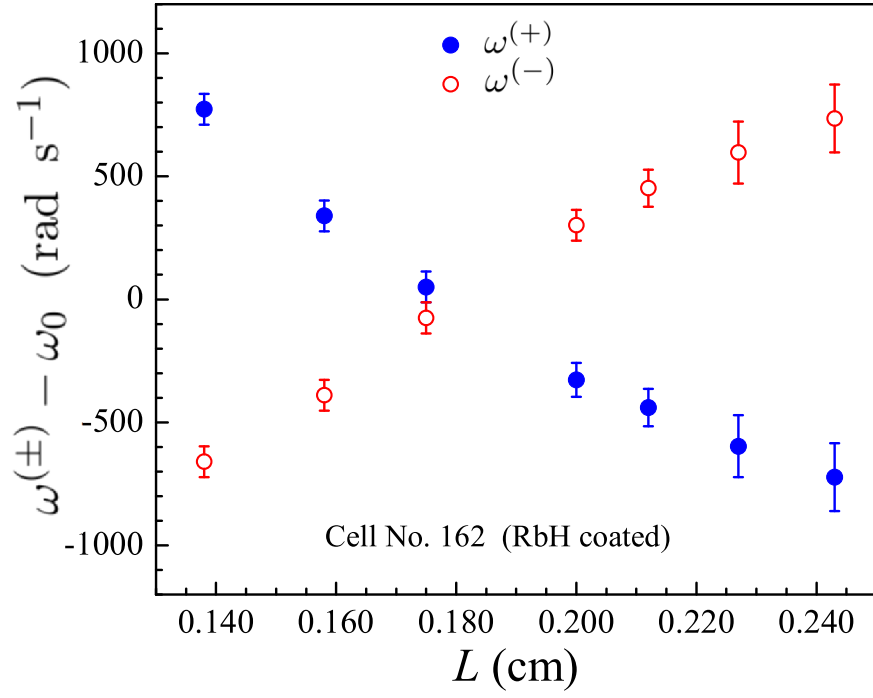
FIG. 4.3. The dependence of the measured EPR frequency shifts $\omega^{(-)} - \omega_o$ (open circles) and $\omega^{(+)} - \omega_o$ (filled circles) on the cell length L. The experimental conditions for the data in Fig 4.3 and Fig. 4.4 are the same and are described in the text.
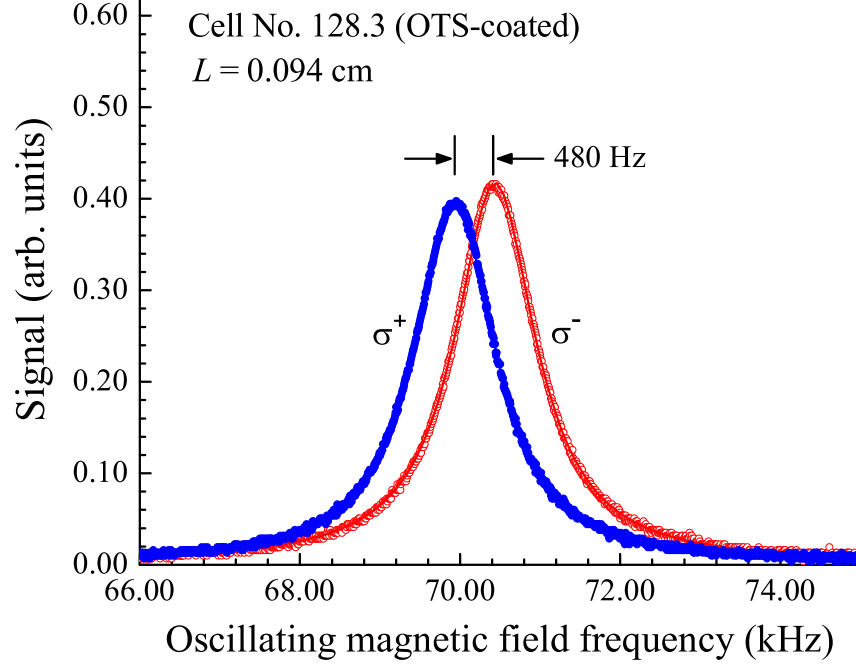
FIG. 4.4. The measured EPR curves in an OTS-coated cell under the same experimental conditions as in Fig.4.3. The OTS-coated cell has the same N_2 density as the RbH-coated cell. The left curve corresponds to σ^+ pumping and therefore $\omega^{(+)}$. The right curve corresponds to σ^- pumping and therefore $\omega^{(-)}$. The shift between these two curve is equal to twice the light shift.

EPR frequencies $\omega^{(-)}$ and $\omega^{(+)}$ that $\Delta = $ -$2\pi \times$ 228 rad s^{-1} (see Fig.4.3). Therefore

$\delta\omega_s = (-\Delta - 2\delta\omega_{light})/2 = 2\pi \times$ 354 rad s^{-1} or 354 Hz. The EPR frequency shifts due

to wall collisions calculated in this way for each cell length L are given in Table III.

Table III. EPR frequency shifts $\delta\omega_s/2\pi$ due to wall collisions in the RbH-coated cell.

Cell length L (cm)	0.138	0.158	0.175	0.200	0.212	0.227	0.243
$\delta\omega_s/2\pi$ (Hz)	354	298	250	190	169	145	124

Therefore, using the $\delta\omega_s$ shown in Table III for each L, we can numerically solve

Eq.(2.24) and Eq.(2.26) for u'_o and u''_o, from which we obtain $\delta\phi_s$ from Eq.(2.27). We

plot in Fig.4.5 the numerically calculated $\delta\phi_s$ for each L. The computed values of $\delta\phi_s$

increases with L. This is because the wall relaxation rate increases with decreasing L,

and therefore the ^{87}Rb vapor and consequently the surface polarization, as well as, $\delta\phi_s$, decreases with decreasing L. This is also consistent with the experimental observation that the Faraday rotation signal which is proportional to the Rb vapor polarization, decreases with decreasing L. In spite of the large error bars, the phase shift $\delta\phi_s$ seems to display saturation behavior as L increases. Physically this is probably due to the following reason. When L is sufficiently large, the contribution to the total relaxation rate from wall interaction becomes negligible, and the ^{87}Rb vapor polarization and consequently the wall polarization, as well as $\delta\phi_s$, becomes independent of L.
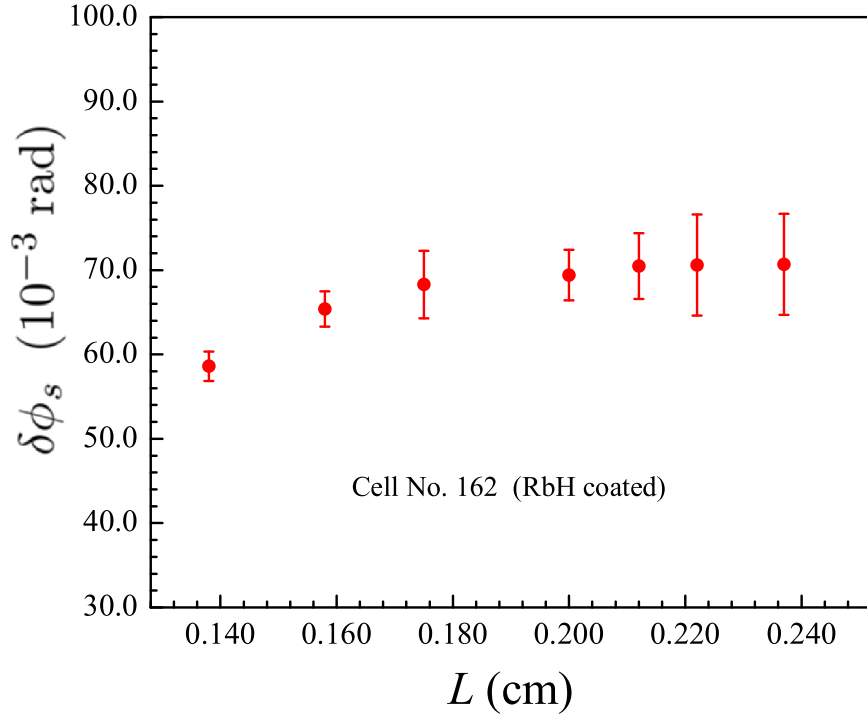

FIG. 4.5. The dependence of the numerically calculated average phase shift $\delta\phi_s$ on the cell length L.

4.2.2 Broadening due to the Oscillating Magnetic Field (rf Broadening)

In discussing the Faraday rotation signal in section 2.3.2, we neglected the spin relaxation. If we include relaxation due to other processes, the Faraday rotation signal is given by [42]

$$S \sim \frac{\omega_1^2}{(\omega_0 - \omega)^2 + \omega_1^2 + \Gamma^2} \,,$$

(4.3)

where $\omega_1 = \gamma B_1$ is proportional to the oscillating magnetic field amplitude and Γ is the relaxation rate due to other processes. One sees from Eq.(4.3) that in the presence of the oscillating magnetic field the linewidth $\Delta \omega_{1/2}$ is given by

$$\Delta \omega_{1/2}^2 = \Gamma^2 + \omega_1^2$$

(4.4)

The load resistor in the circuit that fed the ac current into the rf coils was adjusted so that the variation in the impedance of the circuit during the scan of the EPR curves was insignificant. Thus the voltage V applied to the rf circuit by the function generator was proportional to the amplitude of the oscillating magnetic field. This was further checked using a small pickup coil at the cell location. Therefore Eq.(4.4) can be written as

$$\Delta \omega_{1/2}^2 = \Gamma^2 + a^2 V^2$$

(4.5)

where we have written $\omega_1 = aV$. In order to obtain Γ we measured the EPR linewidth for four different voltages applied to the rf circuit. We plot the square of the linewidth, $\Delta\omega_{1/2}^2$, against the square of the voltage. The square root of the intercept yields Γ, the relaxation rate in the absence of rf broadening. Thus $\Gamma/2\pi = 2.37$ kHz.
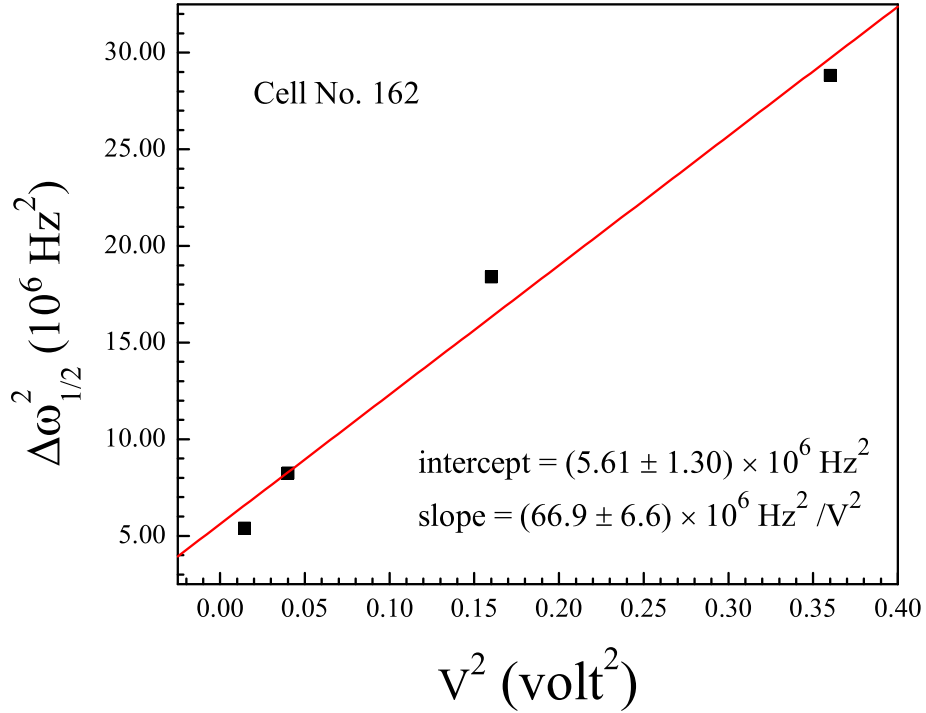

FIG. 4.6. In a RbH-coated cell the linewidths of the EPR curves was measured for four different voltages applied to the rf circuit.

4.2.3 Paramagnetic Impurities

It is important to address the possibility that paramagnetic impurities on the surface such as F-centers could play a significant role in the observed frequency shift. This possibility can be ruled out as described in the following. Paramagnetic F-centers are

known to form when alkali salt is heated in the presence of alkali vapor. We were able to notice the formation of F-centers in the coating by the observance of a slight darkening of the salt-coated cell, which was seen in the cell after ~ 1 year. Although, we did observe F-centers over time, the frequency shift did not noticeably change. There are two physical reasons as to why the F-centers are not contributing to the observed frequency shift. First, due to the fact that we heat up and cool down the cell slowly, the F-centers in the coatings can be reasonably considered to be in thermal equilibrium. More entropy is gained if the F-center is in the bulk of the coating than on the surface because thermodynamics does not favor surface F-centers. Since the Rb atoms that contribute to the signal in our experiment only interact with the salt surfaces, those Rb atoms do not interact with the F-centers in the bulk. Second, the T_1 of the F-centers in RbH, if we assume it is comparable to that in the much-studied alkali halides, is $\sim 10^{-5}$ sec [67], about four orders of magnitude shorter than the T_1 of Rb^+ nucleus in the RbH salt. Therefore the F-center electrons are most likely not polarized, and consequently cannot cause frequency shift.

It is well known that Rb atoms in the vapor can very easily adsorb on the walls if precaution is not taken, and then become paramagnetic impurities. A detailed study was made of this phenomenon [68]. To avoid these adsorbed Rb atoms it is very important to always keep the cell body at a higher temperature, say 10° C or more, than the stem, where the Rb metal is, and it is equally or more important to maintain this temperature difference during (1) the heating-up so that Rb atoms will

not evaporate from the stem and deposit on the cell walls and (2) the cooling-down

so as to make sure the Rb atoms will have time to diffuse to the coldest place, i.e. the

stem. In our experiment we maintain the body and stem temperature difference to

be more than 10 degrees, and the cooling-down time of the cell typically takes more

than five hours. Therefore the average time for a Rb atom to diffuse to the coldest

spot (stem) is of the order of $(4 \, \text{cm})^2/30 \, \text{cm}^2 \, \text{sec}^{-1} = 1$ sec. Therefore during the

cooling down and heating up time Rb atoms can easily reach the coldest spot, the

stem, and will not condense on the cell walls.

4.2.4 Spin Diffusion

In contrast to DNP in which the polarization is generated in the bulk, for RbH the

polarization is generated on the surface. The polarization propagates into the bulk

through spin diffusion. Spin diffusion has been studied in connection with the spin

lattice relaxation [69–71]. Bloembergen showed that the spin diffusion constant is

given by [69]

$$D = W a^2 \approx a^2/50T_1 \qquad (4.6)$$

where W is the spin-exchange probability between two neighboring spins in a crystal,

a is the distance between two spins, and T_1 is the longitudinal relaxation time. Using

$a = 2 \times 10^{-8}$ cm and $T_1 = 10^{-5}$ sec he finds the spin diffusion constant to be $D \approx$

10^{-12} cm^{2}sec^{-1}.

The diffusion length is $\sim \sqrt{DT_1}$, where $D \sim 10^{-12}$ cm^2 s^{-1} is the spin diffusion constant [69] and T_1 is the spin lattice relaxation constant. For CsH , $T_1 \sim 100$ s and therefore the diffusion length λ_D is $0.1\,\mu$m. Using an NMR spectrometer the Princeton group found the average bulk polarization to be 4 times the thermal polarization, which is

$$\langle K_z \rangle_{\text{thermal}} = \frac{21}{4} \frac{\gamma_n \hbar B}{kT} = 3.3 \times 10^{-5} \tag{4.7}$$

Because the spin diffusion length is two orders of magnitude smaller than the sample thickness, the polarization near the surface of the cesium hydride salt is 100 times larger than the polarization measured by the NMR spectrometer.

For RbH $T_1 \sim 0.1$ s and therefore λ_D is 30 times smaller than for CsH. Thus, in the RbH coating the polarization is contained in a surface layer about 30 angstrom thick, and consequently the surface is easier to be saturated than for the CsH coating.

4.2.5   EPR Frequency Shift in the Absence of Light

In the experiment described above, the measured EPR frequency shift includes the contribution due to collisions with polarized walls as well as that due to the Stark effect. We devised an experimental method to be described in the following, which for all practical purposes eliminates the contribution due to the light shift. The frequency shift due to wall collisions observed using this method is larger since it is not offset by the light shift, which has opposite sign.

In this case, the Rb vapor can be pumped either from $F = 1$ level only or from

both $F = 1$ and $F = 2$ levels because the light shift makes negligible contribution to the EPR frequency. To make sure that the observed frequency shift that had the same sign as the helicity of the pump light was not due to light shift but due to wall collisions, we also made sure that the $F = 2$ pump beam caused a negative light shift by slightly detuning it to the high frequency side of the resonance. As one would expect, when the vapor was pumped from both $F = 1$ and $F = 2$ levels, a larger frequency shift was observed. This is due to the fact that the surface polarization of the RbH salt is much larger due to the increased vapor polarization from two beam pumping. The pump beams passed through an optical chopper, rotating at a frequency of 2 Hz, and were blocked by the chopper for about 20 ms during each cycle (see Fig. 4.7(a)). A weak s-polarized evanescent probe beam was used to detect the polarization of the ^{87}Rb vapor. This was done by applying a weak oscillating magnetic field, amplitude-modulated at 2 kHz along the y-axis. The oscillating magnetic field induced Zeeman transitions in the $F = 2$ level. Both the evanescent probe beam and the oscillating magnetic field were always on. The time constant of the lock-in amplifier was 3 ms. This time constant was dictated by the signal-to-noise ratio. The signal had to be averaged 30 times when using a 3 ms time constant. Frequencies of the oscillating magnetic field that were further away from the peak frequency of the EPR curve especially needed to be averaged in order to obtain a sufficiently good signal-to-noise ratio. We stepped the oscillating magnetic field frequency ω and recorded the Faraday rotation signal as a function of time (Fig. 4.7(b)) for each of

these frequencies. We used the same method as described in section 2.41 in order to obtain the Faraday rotation signal.

As the pump beams were unblocked the angular momentum of the ^{87}Rb vapor was transfered to the RbH walls and the Faraday rotation signal started to recover, eventually reaching the equilibrium value $S_\infty(\omega)$.

The EPR frequencies of ^{87}Rb atoms were measured by stepping the oscillating magnetic field frequencies across the Zeeman resonance line. We note that at the equilibrium value $S_\infty(\omega)$ the Faraday rotation signal is at its maximum and the plot of $S_\infty(\omega)$ versus ω yields the usual magnetic resonance line in the presence of the pump beam. The decay part of the signal corresponds to the time period in which the pump beam is blocked (the red segment of the signal in Fig. 4.7(b)). We chose a point $S_t(\omega)$ on this segment of the decay signal for each frequency ω of the oscillating magnetic field. This resulted in the magnetic resonance curves in the absence of the light shift. Each point analyzed on the decay signal for each ω was chosen such that the same amount of time t passed once the pump light was blocked ($t = 0$). By plotting each of these points against the corresponding frequency ω of the oscillating magnetic field we obtained EPR curves in the absence of light shift. The EPR curves obtained using this method for σ^+ and σ^- pumping light are shown in Fig.4.8 - 4.10. The EPR curves in Fig. 4.8 and Fig. 4.9 used one beam pumping whereas the EPR curves in Fig. 4.10 were obtained with two beam pumping. The fact that the EPR frequency shift is larger in Fig. 4.10 is consistent with the fact that two beam pumping

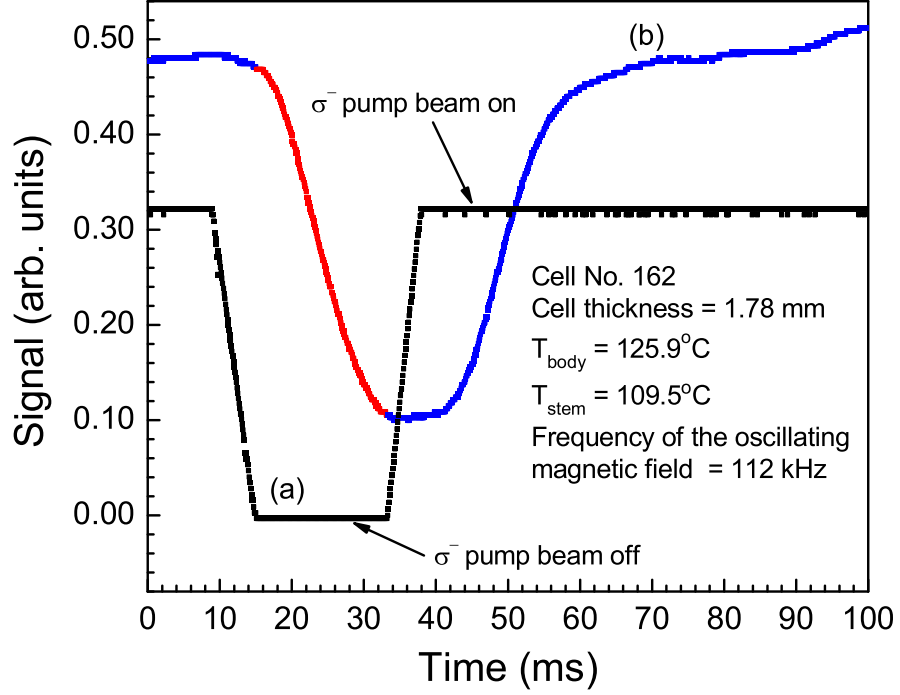produces high vapor polarization and therefore larger wall polarization.

FIG. 4.7. The resonance signal as the pump beam is being chopped. As the pump beam is blocked the signal decays until the pump beam is unblocked.

To more clearly understand how this method nearly eliminates the contribution from the light shift, we consider the phase shift accumulated by these ^{87}Rb atoms when the pump beams are blocked at $t = 0$ which is $\delta\omega_{\text{light}}(-T)$, where the ^{87}Rb atoms that were polarized at time T ($T < 0$) would begin to accumulate phase shift due to the light until the pump beams were blocked at $t = 0$. Thus, at time t the probability for these ^{87}Rb atoms to maintain polarization is $e^{-(t-T)/\tau_{Rb}}/\tau_{Rb}$, and so the average phase shift due to light shift at time t is given by

$$\delta\phi_{\text{light}} = \int_{-\infty}^{0} dT \, \delta\omega_{\text{light}}(-T)e^{-(t-T)/\tau_{Rb}}/\tau_{Rb} = \delta\omega_{\text{light}}\tau_{Rb}e^{-t/\tau_{Rb}} \tag{4.8}$$

We can make the following interpretation from Eq.(4.8). We can consider the moment when the pump beams are blocked, at $t = 0$, in which case, from Eq.(4.8), we find that the average phase shift of Rb atoms due to light shift is $\delta\omega_{\text{light}}\tau_{Rb}$. As $t > 0$ there is no longer any additional contribution to the phase shift due to the Stark effect, thus as time goes to t the phase shift decays as $e^{-t/\tau_{Rb}}/\tau_{Rb}$. Moreover, we deduce that the average phase shift due to the Stark effect is zero, in that the points we select on the decay section of the signal in Fig. 4.7(b) (in order to obtain our EPR curves) are $t > 10$ ms and $\tau_{Rb} \sim 10^{-4}$ s.

We have found that the EPR frequency shift due to collisions with polarized walls increased with the density of the Rb vapor and the power of the pump laser as shown in Fig. 4.11 and Fig. 4.12. This can be understood as follows. The frequency shift due to wall collisions is proportional to the wall nuclear polarization, which in turn is proportional to the angular momentum flux into the surface. This angular momentum flux into the surface increased with the density and polarization of the Rb vapor. The latter increased with the power of the pump beam.
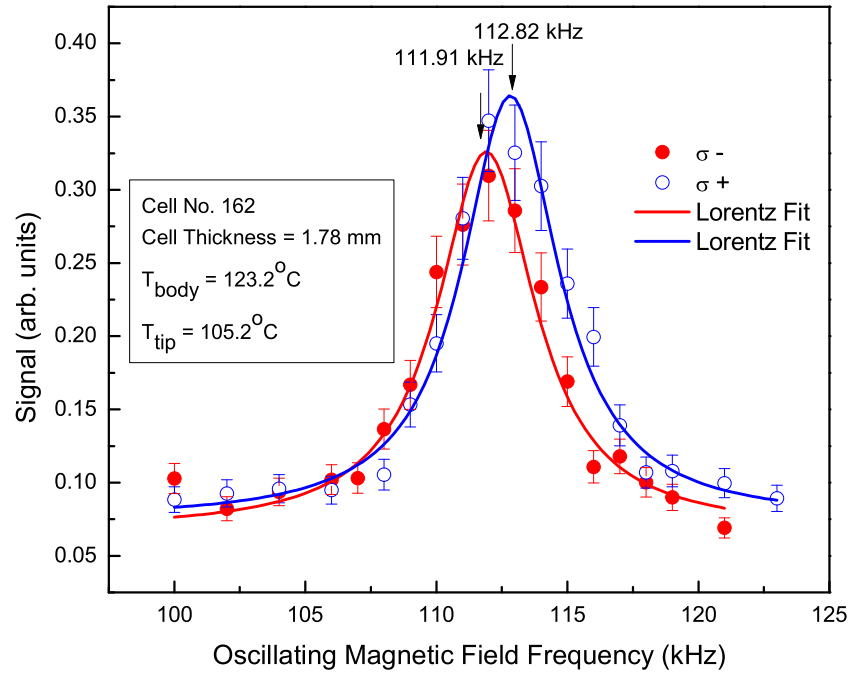
FIG. 4.8. The EPR curves for σ^+ and σ^- pumping light, where only $F = 1$ pumping was used. The curves were analyzed on the decay part of the signal in Fig. 4.7(b) after the pump beam was blocked. The EPR frequency shift $\Delta = 910$ Hz.
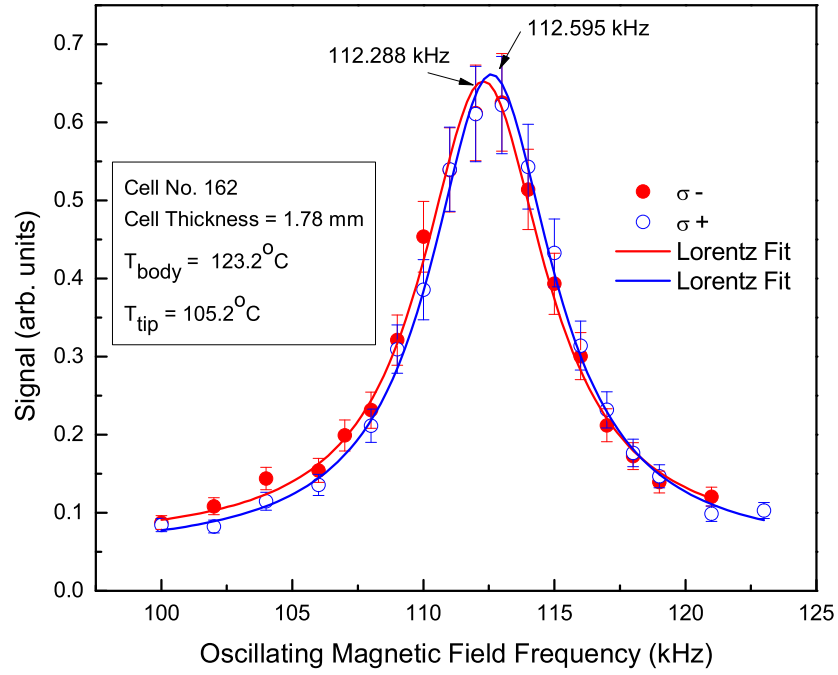
FIG. 4.9. The EPR curves for σ^+ and σ^- pumping light, where only $F = 1$ pumping was used. The curves were analyzed on the plateau part of the decay signal in Fig. 4.7(b) when the pump beam was unblocked and the signal was at a maximum. The EPR frequency shift $\Delta = 307$ Hz.
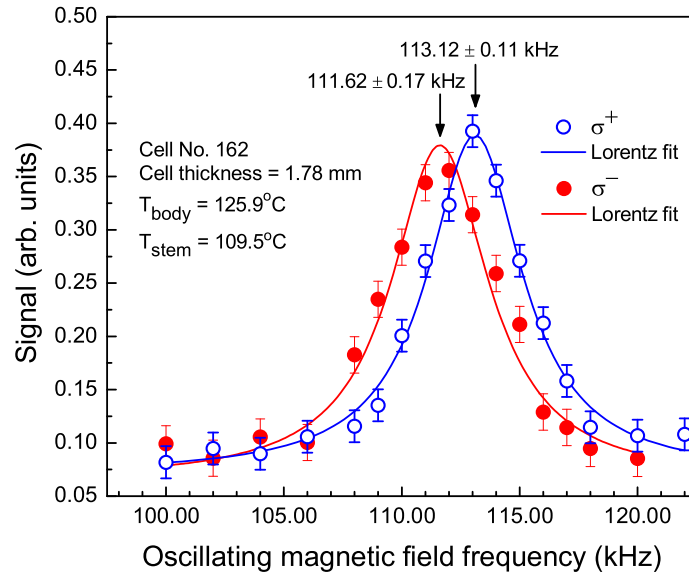
FIG. 4.10. A representative set of EPR curves from an RbH-coated cell. The signal was obtained by pumping from both $F = 1$ and $F = 2$ level. The open circles represent the resonance curve with σ^+ pumping light and the filled circles represent the resonance curve with σ^- pumping light.
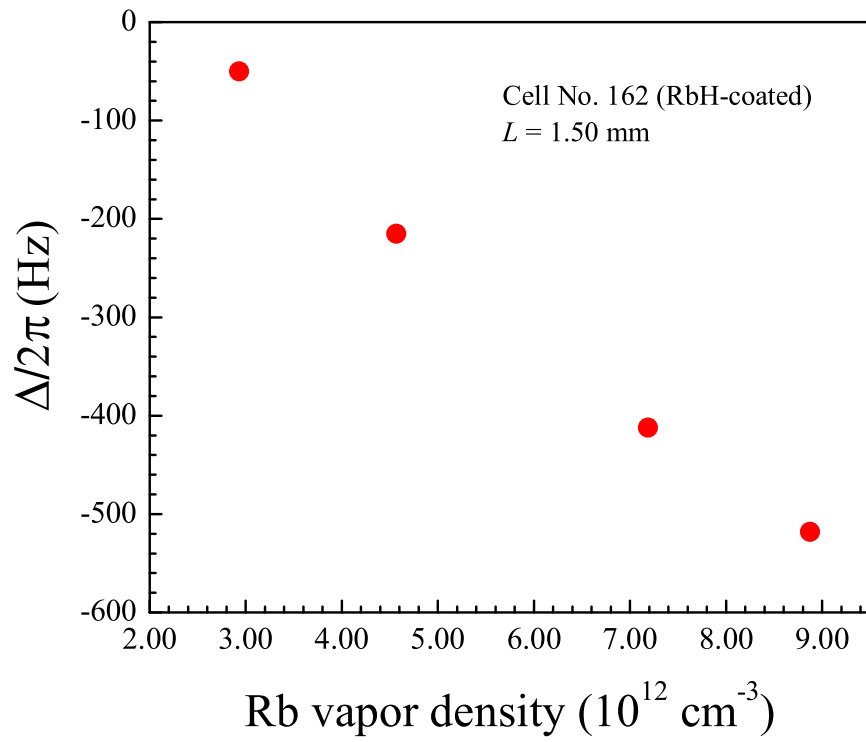
FIG. 4.11. The linear dependence of $\Delta/2\pi$ on density where the density is increased by increasing the temperature of the reservoir in which the Rb metal is held.
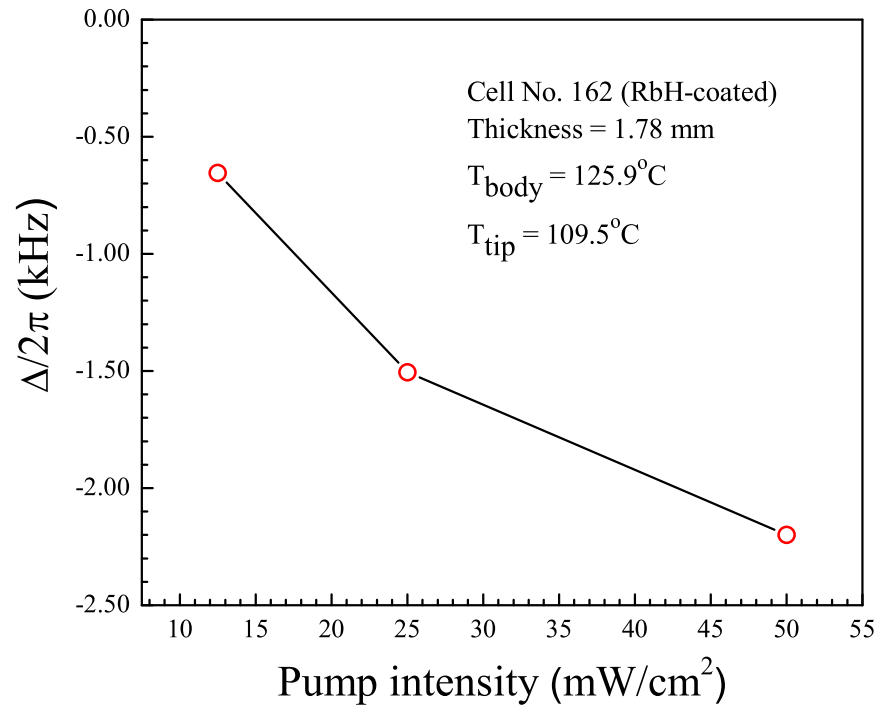
FIG. 4.12. The dependence of $\Delta/2\pi$ on pump intensity.

Chapter 5

Conclusion

Wall interactions play an important role in many atomic physics experiments. They are one of the main spin relaxation mechanisms. Wall interactions can also cause a shift in the magnetic resonance frequency. In this dissertation I studied wall interactions on two types of surfaces: antirelaxation coatings and alkali hydride (RbH) salt. The focus of my studies is on the frequency of the electron paramagnetic resonance of the gas phase ^{87}Rb atoms due to the wall interactions. A non-traditional method was used for these studies. I measured the EPR frequencies for $\sigma^{(+)}$ and $\sigma^{(-)}$ pumping in a cell of variable length. The typical cell length is ~ 0.1 cm. One important feature of the experiment is the use of an evanescent beam to probe the Rb vapor polarization.

In antirelaxation-coated cells the dependence of the measured EPR frequency on cell length allowed me to extract the average dwell time τ_s of a spin polarized Rb atom on the OTS and paraffin surfaces. The dwell time τ_s was found to be of the order of

$1\,\mu s$, significantly longer than the value reported in the literature. The measured long dwell time was attributed to the porous nature of the antirelaxation coating, which is typically composed of saturated long hydrocarbon chains. At a cell temperature of 72°C the dwell times for OTS- and paraffin-coated walls are $0.9 \pm 0.1\ \mu s$ and $1.8 \pm 0.2\ \mu s$, respectively. Since the relaxation probability on OTS is about one order of magnitude larger than that on paraffin, the observation of a longer dwell on paraffin seems to indicate that the average strength of the interactions experienced by the Rb atoms while they are inside OTS is much stronger than the interactions they experience while inside paraffin.

In RbH-coated cells, the surface of the RbH salt was nuclear spin polarized by spin exchange with optically pumped Rb vapor. In these cells I observed a large shift ($\sim$ several hundred Hz) in the EPR frequency of the gas phase ^{87}Rb atoms in a millimeter-sized cell. By measuring the dependence of the EPR frequency shifts on the cell length and by comparing the EPR frequency shifts in RbH-coated cells with those in OTS-coated cells, I provided convincing evidence that the observed EPR frequency shift is due to collisions with RbH-coated walls and not due to gas phase processes. The observed EPR frequency shift is due to the Fermi contact interaction between the s-electron of the adsorbed ^{87}Rb atom and the polarized nucleus on the RbH salt surface. The measured EPR frequency shifts allowed us to calculate the ensemble-averaged phase shift $\delta\phi_s$ experienced by the Rb atom while adsorbed on the walls. Under our experimental condition $\delta\phi_s$ is about 70 mrad.

The frequency shift due to quadrupole wall interaction causes a splitting of the magnetic resonance line, which could lead to line broadening if different magnetic resonance component lines are not resolved. Magnetic hyperfine interaction, on the other hand, as far as frequency shift is concerned, is equivalent to a magnetic field acting on the spin polarized atoms. Therefore it can cause a systematic error in the magnetic resonance frequency. Since the frequency shift due to wall collisions, unlike that due to gas phase collisions, increases with decreasing cell size, this systematic error in the magnetic resonance frequency, the magnitude of which has yet to be determined, may not be completely negligible in high precision miniature atomic magnetometry. Even though the Fermi contact wall interaction does not directly cause a line broadening, indirectly it can through the following mechanism. The equivalent magnetic field depends on the wall polarization, which in turn depends on factors such as the power of the laser that pumps the alkali vapor. Therefore, fluctuations in the laser power can potentially cause fluctuations in the wall polarization, leading to a fluctuation in the equivalent magnetic field and consequently a broadening of the magnetic resonance lines.

Bibliography

[1] F. P. Calaprice, W. Happer, D. F. Schreiber, M. M. Lowry, E. Miron, and X. Zeng. Nuclear alignment and magnetic moments of ^{133}Xe, ^{133}Xe^m, and ^{131}Xe^m by spin exchange with optically pumped ^{87}Rb. *Physical Review Letters*, 54:174 1985; M. Kitano, F. P. Calaprice, M. L. Pitt, J. Clayhold, W. Happer, M. Kadar-Kallen, M. Musolf, G. Ulm, K. Wendt, T, Chupp, J. Bonn, R. Neugart, E. Otten, and H. T. Duong. Nuclear orientation of radon isotopes by spin-exchange optical pumping. *Physical Review Letters*, 60:2133 1988.

[2] T. E. Chupp R. J. Hoare, R. A. Loveman, E. R. Oteiza, J. M. Richardson, and M. E. Wagshul. Results of a new test of local lorentz invariance: a search for mass anisotropy in ^{21}Ne. *Physical Review Letters*, 63:1541 1989.

[3] M. S. Albert, G. D. Cates, B. Driehuys, W. Happer, C. S. Springer, Jr., B. Saam, and A. Wishnia. Biological magnetic resonance imaging using laser-polarized ^{129}Xe. *Nature London*, 370:199 1994.

[4] H. Middleton, R. D. Black, B. Saam, G. D. Cates, G. P. Cofer, R. Guenther, W. Happer, L. W. Hedlund, G. A. Johnson, K. Juvan. MR imaging with hyperpolarized ^{3}He gas. *Magnetic Resonance in Medicine*, 33:271-5, 1995.

[5] G. Cocconi and E. Salpeter. A search for anisotropy of inertia. *Nuovo Cimento*, 10:646 1958.

[6] V. W. Hugh, H. G. Robinson, and V. Beltran-Lopez. Upper limit for the anisotropy of inertial mass from nuclear resonance experiments. *Physical Review Letters*, 4:342 1960.

[7] R. W. P. Drever. A search for anisotropy of inertial mass using a free precession technique. *Philosophical Magazine*, 6:683 1961.

[8] D. Budker and M. Romalis. Optical magnetometry. *Nature Physics*, 3:227 2007.

[9] I. K. Kominis, T. W. Kornack, J. C. Allred and M. V. Romalis. A subfemtotesla multichannel atomic magnetometer. *Nature*, 422:596 2003.

[10] P. D. D. Schwindt, B. Lindseth, S. Knappe, V. Shah, and J. Kitchingb. Chip-scale atomic magnetometer with improved sensitivity by use of the M_x technique. *Applied Physics Letters*, 90, 081102 2007.

[11] M. V. Balabas, D. Budker, J. Kitching, P. D. D. Schwindt, and J. E. Stalnaker. Magnetometry with millimeter-scale antirelaxation-coated alkali-metal vapor cells. *Journal of Optical Society of America B*, 23:1001 2006.

[12] K. F. Zhao and Z. Wu. Evanescent wave magnetometer. *Applied Physics Letters*, 89:261113 2006.

[13] S. Knappe, V. Shah, P. D. D. Schwindt, L. Hollberg, J. Kitching, L.-A. Liew, and J. Moreland. A microfabricated atomic clock. *Applied Physics Letters*, 85:1460 2004.

[14] H. G. Robinson and C. E. Johnson. Narrow ^{87}Rb hyperfine-structure resonances in an evacuated wall-coated cell. *Applied Physics Letters*, 40:771 1982.

[15] D. Budker, V. Yashchuk and M. Zolotorev. Nonlinear magneto-optic effects with ultranarrow widths, *Physical Review Letter*, 81:5788 1998.

[16] W. Wasilewski, K. Jensen, H. Krauter, J. J. Renema, M.V. Balabas, and E. S. Polzik. Quantum noise limited and entanglement-assisted magnetometry. *Physical Review Letter*, 104:133601 2010.

[17] W. C. Griffith, M. D. Swallows,T. H. Loftus, M.V. Romalis, B. R. Heckel, and E. N. Fortson. Improved limit on the permanent electric dipole moment of ^{199}Hg. *Physical Review Letter*, 102:101601 2009.

[18] M. A. Bouchiat and J. Brossel. Relaaxation of optically pumped Rb atoms on paraffin-coated walls. *Physical Review*, 147:41 1966.

[19] S. J. Seltzer, D. J. Michalak, M. H. Donaldson, M. V. Balabas, S. K. Barber, S. L. Bernasek, M.-A. Bouchiat, A. Hexemer, A. M. Hibberd, D. F. Jackson Kimball, C. Jaye, T. Karaulanov, F. A. Narducci, S. A. Rangwala, H. G. Robinson, A. K. Shmakov, D. L. Voronov, V. V. Yashchuk, A. Pines, and D. Budker. Investigation of antirelaxation coatings for alkali-metal vapor cells using surface science techniques. *Journal of Chemical Physics*, 133:144703 2010.

[20] K. F. Zhao, M. Schaden, and Z. Wu. Method for measuring surface-interaction parameters of spin-polarized Rb atoms on coated Pyrex glass surfaces using edge enhancement. *Physical Review A*, 78:034901 2008.

[21] S. R. Schaefer, G. D. Cates, Ting-Ray Chien, D. Gonatas, W. Happer, and T. G. Walker. Frequency shifts of the magnetic-resonance spectrum of mixtures

of nuclear spin-polarized noble gases and vapors of spin-polarized alkali-metal atoms. *Physical Review A*,39:5613 1989.

[22] W. Happer. Optical pumping. *Review of Modern Physics*, 44:169 1972.

[23] S. P. Dmitriev and N. A. Dovator. Frequency shift of the magnetic resonance in $5_s^2 S_{1/2}$ rubidium atoms due to spin-exchange collisions with optically oriented cesium atoms. *Technical Physics*, 52:940 2007.

[24] J. H. Simpson, Bull. Am. Phys. Soc. 23:394 1978.

[25] C. H. Volk, J. G. Mark, and B. Grover. Spin dephasing of Kr^{83}. *Physical Review A*, 20:2381 1979.

[26] T. M. Kwon, J. G. Mark, and C. H. Volk. Quadrupole nuclear spin relaxation of ^{131}Xe in the presence of rubidium vapor. *Physical Review A*, 24:1894 1981.

[27] C. Cohen-Tannoudji, J. Phys. (Paris) 24:653 1963.

[28] Z. Wu, W. Happer, and J. Daniels. Coherent nuclear-spin interactions of adsorbed ^{131} Xe gas with surfaces. *Physical Review Letters*, 59:1480 1987; Z. Wu *et al.*, *Physical Review*, A37:1161 1988.

[29] K. Ishikawa, B. Patton, Y.-Y. Jau, and W. Happer. Spin transfer from an optically pumped alkali vapor to a solid. *Physical Review Letters*, 98:183004 2007.

[30] K. Zhao and Z. Wu. Hyperfine polarization and its normal gradient coefficient of ^{87}Rb atoms in the vicinity ($\sim 10^{-5}$cm) of coated and uncoated pyrex glass surfaces.*Physical Review Letters*, 91:113003 2003.

[31] K. Zhao and Z. Wu. Regionally specific hyperfine polarization of Rb atoms in the vicinity ($\sim 10^{-5}$cm) of surfaces. *Physical Review A*, 71:012902 2005.

[32] M. Schaden, K. Zhao and Z. Wu. Effects of diffusion and surface interactions on the line shape of electron paramagnetic resonances in the presence of a magnetic field gradient. *Physical Review A* 76:062502 2007; 77:049903(E) 2008.

[33] K. F. Zhao and Z. Wu. Evanescent wave magnetometers with ultrathin ($\sim$ 100μm) cells. *Applied Physics Letters*, 93:101101 2008.

[34] We note that the coefficients in the definitions of μ and η in Eq.(2.3) and Eq.(2.4) are different from those in [32]. The reason for this discrepancy is that the boundary conditions in [32] were derived using a simple hopping model, whereas the coefficients in Eq.(2.3) and Eq.(2.4) are chosen so that the theory agrees with the gas kinetic theory for the EPR frequency shift when $\mid \mu \mid \ll 1$.

[35] E. Ulanski and Z. Wu. Measurement of dwell times of spin polarized rubidium atoms on octadecyltrichlorosilane- and paraffin-coated surfaces. *Applied Physics Letter*, 98:201115 2011.

[36] K. F. Zhao, M. Schaden, and Z. Wu. Enhanced magnetic resonance signal of spin-polarized Rb atoms near surfaces of coated cells. *Physical Review A*, 81:042903 2010.

[37] Z. Wu, S. Schaefer, G.D. Cates, and W. Happer, *Physical Review A*, 37:1161 1988.

[38] F. Masnou-Seeuws and M. A. Bouchiat, *Journal de Physique* 28:406 1967.

[39] G. K. Woodgate. Elementary Atomic Structure. *Oxford University Press*, 1980.

[40] C. P. Slichter. Principle of Magnetic Resonance. *Springer-Verlag*, 1980.

[41] L. Allen and J. H. Eberly. Optical resonance and two-level atoms. *Dover Publications*, 1987.

[42] See, for example, C. Cohen-Tannoudji, B. Diu, and F. Laloe. Quantum mechanics. Wiley,New York, 1977.

[43] R. Knize, Z. Wu, and W. Happer. Advances in Atomic and Molecular Physics. vol. 24, p. 223 - 267. *Academic Press*, 1988.

[44] R. A. Bernheim. Spin relaxation in optical pumping. *Journal of Chemical Physics*, 36:135 1962.

[45] R. M. Herman. Theory of spin exchange between optically pumped rubidium and foreign gas nuclei. *Physical Review*, 137:1062 1965.

[46] T. Walker and W. Happer. Spin exchange optical pumping of noble-gas nuclei.*Review of Modern Physics*, 69:629 1997.

[47] B. Patton, Ph.D. dissertation, Princeton University, 2007.

[48] T. G. Walker. Estimates of spin-exchange parameters for alkali-metal-noble-gas pairs. *Physical Review A*, 40:4959 1989.

[49] J. A. Bearden and A. F. Burr. Reevaluation of x-ray atomic energy levels. *Review of Modern Physics*, 39:125 1967.

[50] W. Weyhmann and F. M. Pipkin. Optical absorption spectra of alkali atoms in rare-gas matrices. *Physical Review*, 237:A490 1965.

[51] E. Lundgren, M. Qvarford, R. Nyholm, and J. N. Anderson. Alkali core-level binding-energy shifts in alkali/4d-metal interface systems. *Physical Review B*, 50:4711 1994.

[52] E. Lundgren, M. Qvarford, R. Nyholm, and J. N. Anderson. Unified behavior of alkali core-level binding-energy shifts induced by sp metals. *Physical Review B*, 506:12560 1997.

[53] P. H. Citrin, G. K. Wertheim, and Y. Baer. Core-level binding energy and density of states from the surface atoms of gold. *Physical Review Letters*, 41:1425 1978.

[54] J. F. van der Veen, F. J. Himpsel, and D. E. Eastman. Structure-dependent 4fcore-level binding energies for surface atoms on Ir(111), Ir(100)-(5 × 1), and metastable Ir(100)-(1×1). *Physical Review Letters*, 44:189 1980.

[55] D. Briggs and M. P. Seah. Practical surface analysis by auger and x-ray photo-electron spectroscopy, *John Wiley*, New York, 1983.

[56] Z. Wu, private communication.

[57] M. S. Rosen, T. E. Chupp, K. P. Coulter, R. C. Welsh, and S. D. Swanson. Polarized ^{129}Xe optical pumping/spin exchange and delivery system for magnetic resonance spectroscopy and imaging studies. *Review of Scientific Instruments*, 70:1546 1999.

[58] E.B. Alexandrov, M.V. Balabas, D. Budker, D. English, D.F. Kimball, C.-H. Li, and V.V. Yashchuk. Light-induced desorption of alkali-metal atoms from paraffin coating. *Physical Review A*, 66:042903 2002.

[59] G. Singh, P. Dilavore, and C. Alley. A technique for preparing wall coated cesium vapor cells. *Review of Scientific Instruments*, 43:1388 1972.

[60] P. J. Thomas, R. Mani, and N. Khalil. Noncontact measurement of etalon spacing using a retroreflection technique. *Review of Scientific Instruments*, 70:2225 1999.

[61] K. F. Zhao, M. Schaden, and Z. Wu. Method for measuring the dwell time of spin-polarized Rb atoms on coated pyrex glass surfaces using light shift. *Physical review Letters*, 103:073201 2009.

[62] Y. W. Yi, H. G. Robinson, S. Knappe, J. E. Maclennan, C. D. Jones, C. Zhu, N. A. Clark, and J. Kitching. Method for characterizing self-assembled monolayers as antirelaxation wall coatings for alkali vapor cells. *Journal of Applied Physics*, 104:023534 2008.

[63] B. Driehuys, G. D. Cates, and W. Happer. Surface relaxation mechanisms of laser-polarized ^{129}Xe. *Physical Review Letters*, 74:4943 1995.

[64] S. N. Atutov et al., *Physcial Review A*, 60:4693 (1999)

[65] A. Cappello et al., *Journal of Chemical Physics*, 127:044706 (2007).

[66] B. S. Mathur, H. Tang, and W. Happer. Lights shifts in the alkali atoms. *Physical Review*, 171:11 (1968); W. Happer and B. S. Mathur. Effective operator formalism in optical pumping. *Physical Review*, 163:12 1967.

[67] A. M. Portis. Electronic structure of F centers: saturation of the electron spin resonance. *Physical Review* 91:1071 1953.

[68] K. F. Zhao and Z. Wu, *Physical Review Letters A*, 299:7378 2002.

[69] N. Bloembergen. On the interaction of nuclear spins in a crystalline lattice. *Physica*, 15:386 1949.

[70] G. R. Khutsishvili. Spin Diffusion. *Soviet Physics Uspekhi*, 87:211 1965.

[71] G. W. Leppelmeier and J. Jeener. Measurement of the nuclear spin diffusion coefficient in CaF_2. *Physical Review*, 175:498 1968.

[72] E. Ulanski and Z. Wu, *Physical Review A*, in press.

Curriculum Vitae

Ulanski, Emily

1984	Born on May 1, in Elizabeth, NJ
1998-2002	Cranford High School, Cranford, NJ
2002-2006	Union College, Schenectady, NY; B.S., majored in Physics, minored in Mathematics
2013-2014	Teaching Assistantship, Rutgers University, Newark, NJ, Department of Physics
2014	Ph. D. in Applied Physics, Rutgers University, Newark, NJ

Publications

2011	Emily Ulanski and Zhen Wu. Measurement of dwell times of spin polarized rubidium atoms on octadecyltrichlorosilane- and paraffin-coated surfaces. *Applied Physics Letters*, 98, 201115.
2012	K. Zhao, E, Ulanski, Z. Wu, and M. Schaden. Dwell Time Measurements of Wall Collisions of Spin Polarized Rb Atoms on Antirelaxation Coatings *Journal of Physics*, 388, 012046.
2014	Emily Ulanski and Zhen Wu. Observation of large frequency shifts of the electron paramagnetic resonance of ^{87}Rb atoms due to collisions with cell walls coated with RbH salt. *Physical Review A*, in press.